

APR 8 1972

MAY 25 1972

OCT 20 1974

AFOSR - TR - 71-2183

PROPERTY OF U.S. AIR FORCE
L-30 IN-MAY
F40600-72-C-0003

AN EXPERIMENTAL INVESTIGATION OF
SUPERSONIC FLOW PAST YAWED CONES

by

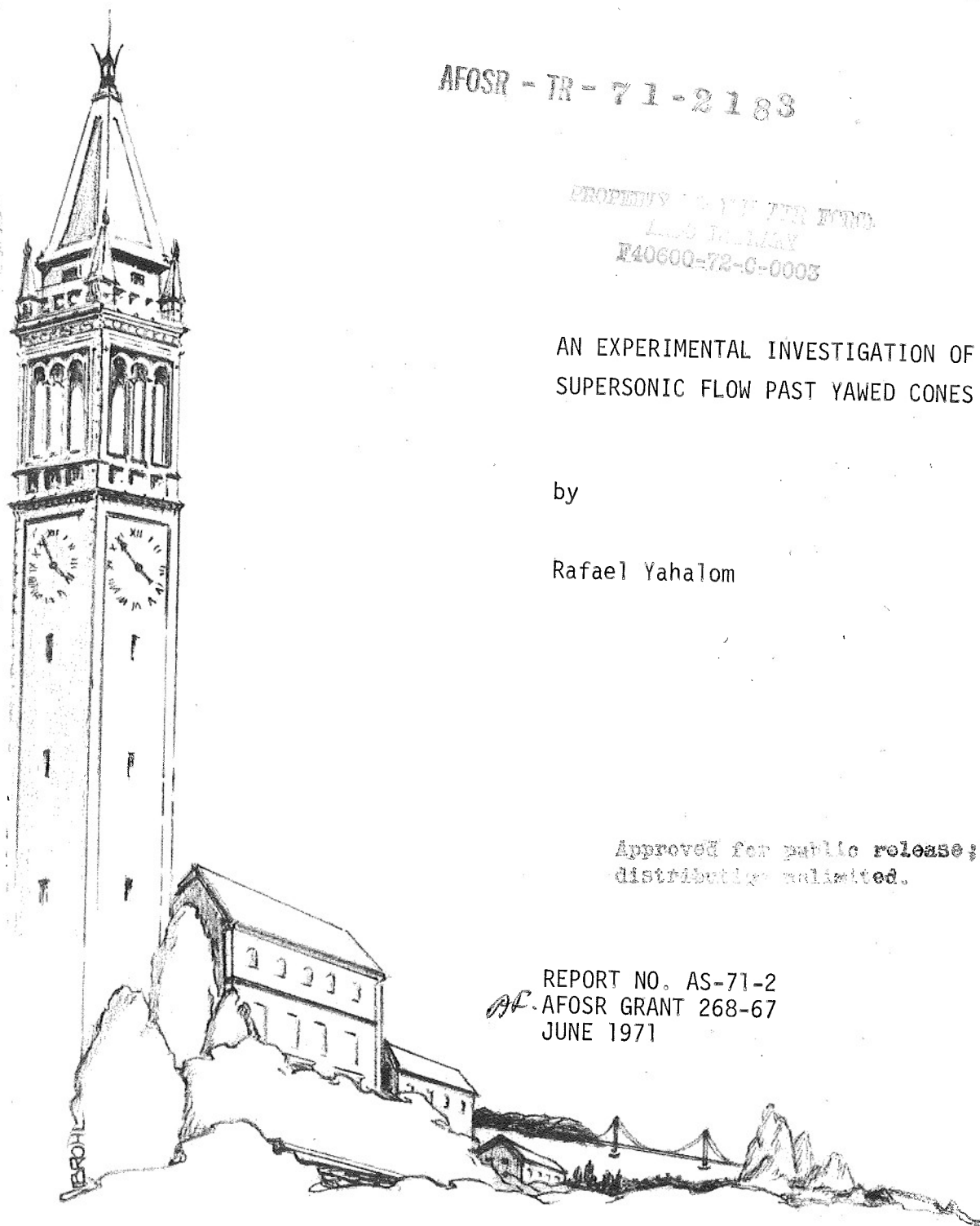
Rafael Yahalom

Approved for public release;
distribution unlimited.

REPORT NO. AS-71-2
AFOSR GRANT 268-67
JUNE 1971

COLLEGE OF ENGINEERING
UNIVERSITY OF CALIFORNIA, Berkeley

PROPERTY OF U.S. AIR FORCE
AEDC LIBRARY
F40600-72-C-0003



AD 728233

AFOSR-TR-71-2183

CONTRACT NO. ^{AF}-AFOSR GRANT 268-67
REPORT NO. AS-71-2
APRIL 1971

SUPPORTED BY
THE UNITED STATES AIR FORCE
OFFICE OF SCIENTIFIC RESEARCH

AN EXPERIMENTAL INVESTIGATION OF
SUPERSONIC FLOW PAST YAWED CONES

by

Rafael Yahalom

1. Yawed cones - Supersonic flow
2. " " " "

*This document has been approved for public release and
sale; its distribution is unlimited.*

Approved for public release;
distribution unlimited.

FACULTY INVESTIGATOR:
M. HOLT, PROFESSOR OF AERONAUTICAL SCIENCES

Aeronautical Sciences Division
University of California
Berkeley, California 94720

ABSTRACT

An experimental investigation of supersonic flow around cones was conducted in the Supersonic Wind Tunnel at the University of California, Berkeley, at a free stream Mach number of 2.72 and Reynolds number per foot of 1.66×10^6 . Three cones of semi-apex angles of 10° , 15° and 20° were investigated at relative incidences α/θ_c up to 3. In addition to measuring surface pressure, a detailed study of the flow in the plane of symmetry $\phi = 180^\circ$ was made by means of a pitot-hot wire probe. The shape of the outer shock wave as well as of the imbedded shocks were determined. Oil and vapor screen techniques and a Schlieren system were used to visualize the flow field.

For moderate angles of yaw $\alpha/\theta_c < 1$, good agreement is found between the theoretical and the experimental results. At higher angles of attack imbedded shocks are formed and two symmetrical vortices are shed on the leeward side of the cones. The concept of the "lifting off" of the vortical singularity appears to be meaningful in real flow and its location is determined.

TABLE OF CONTENTS

	<u>Page</u>
ABSTRACT	i
LIST OF FIGURES	iv
LIST OF SYMBOLS	vi
1.0 INTRODUCTION	1
2.0 EXPERIMENTAL APPARATUS	5
2.1 Wind Tunnel	5
2.2 Models and Supports	5
2.3 Probe	6
3.0 EXPERIMENTAL PROCEDURE AND DATA REDUCTION	8
3.1 Free Stream Condition	8
3.2 Model Setting and Alignment	8
3.3 Surface Pressure Measurements	9
3.4 Flow Field Survey	9
3.4.1 Pitot Survey	10
3.4.2 Hot Wire Measurements	11
3.4.2.1 Hot wire data reduction	11
3.4.2.2 Determination of the velocity direction	14
3.4.2.3 Hot wire experimental procedure	15
3.4.3 Flow Visualization	16
4.0 RESULTS AND DISCUSSION	18
4.1 Surface Pressure Distribution	19
4.2 Oil Flow	21
4.3 Static Forces	22
4.4 Outer Shock Wave	23

4.5	Imbedded Shocks	24
4.6	The Viscous Layer and the Vortex System	25
4.7	The Leeward Meridian Plane $\phi = 180^\circ$	27
4.7.1	The Vortical Singularity	27
4.7.2	The Flow Field in the Plane of Symmetry $\phi = 180^\circ$	30
5.0	CONCLUSIONS AND SUGGESTIONS	33
	REFERENCES	35
	FIGURES	39
	APPENDIX	71

LIST OF FIGURES

1. Coordinate System and Velocity Components
2. Vortical Layer on an Inclined Cone (From Ferri, 1950)
3. Streamline Pattern on a Circular Cone at Moderate to Large Angles of Attack (From Melnik, 1966)
4. Model and Pressure Taps
5. 15° Cone and Tubes
6. 20° Cone with Adapter and Probe
- 7a. Hot-wire-Pitot Probe
- 7b. The Rotating Part of the Hot-Wire Probe
8. Relative Position Between the Velocity Vector and the Hot-Wire in the Plane $\phi = 180^\circ$
9. Color Schlieren of 10° Cone at $\alpha = 30^\circ$
10. Oil Flow over 10° Cone at $\alpha = 30^\circ$
- 11a. Circumferential Pressure Distribution for a $\theta_c = 10^\circ$ Cone at Various Angles of Attack
- 11b,c. Comparison of Experimental Pressure Distribution with Jones' Results
- 11d. Circumferential Pressure Distribution for a $\theta_c = 15^\circ$ Cone at Various Angles of Attack
- 11e. Comparison of Experimental Pressure Distribution with Jones' Results
12. Axial Force Coefficient
13. Normal Force Coefficient
14. Drag Coefficient
15. Lift Coefficient

- 16. Lift to Drag Ratio
- 17a. Outer Shock Shape for 10° Cone at 5° and 10° of Incidence
- 17b. Outer Shock Shape for 10° Cone at 15°, 20°, 25°, 30° of Incidence
- 17c. Outer Shock Wave for 15° Cone
- 17d. Outer Shock Shape for 20° Cone at 5° and 20° of Incidence
- 17e. Outer Shock Shape for 20° Cone at 15°, 20° and 25° of Incidence
- 18. Imbedded Shocks and Viscous Hump
- 19. Maximum Vortex Height θ_V/θ_C
- 20 a-c. Mach Number Component in the θ Direction in the $\phi = 180^\circ$ Plane
- 21a-c. Stagnation Pressure Distribution in Plane of Symmetry $\phi = 180^\circ$
- 22a-c. Static Pressure Distribution in Plane of Symmetry $\phi = 180^\circ$
- 23a. Static Temperature Distribution in Plane of Symmetry $\phi = 180^\circ$
for 10° Cone
- 23b. Static Temperature Distribution in Plane of Symmetry $\phi = 180^\circ$
for 15° Cone
- 23c. Static Temperature Distribution in Plane of Symmetry $\phi = 180^\circ$
for 20° Cone
- 24. Flow Field Around a Cone at a Large Angle of Attack
- A-1. End Loss Correction Factors

LIST OF SYMBOLS

a	local speed of sound
A	angle between probe axis and local velocity vector
C_A	axial force coefficient
C_D	drag coefficient
C_L	lift coefficient
C_N	normal force coefficient
C_p	pressure coefficient
C_{Nu}	hot wire correction factors
C_R	
d	wire diameter
H	cone height
i	electrical current through the wire
k	thermal conductivity
Kn	Knudsen number
ℓ	wire length
M	Mach number
M_{n_1}, M_{n_2}	Mach number components, see Fig. 8
M_θ	Mach number in the θ direction
Nu	Nusselt number
p	pressure
P_{t_2}	Pitot pressure
r	radial coordinate
R	hot wire resistance
Re	Reynolds number
S	parameter defined in Sec. 3.4.2.1

T	temperature
u	radial velocity component
U	velocity
v	normal velocity component, in θ direction
w	azimuthal velocity component
x	distance along cone generator

Greek Letters

α	angle of attack
α_M	local velocity vector direction, see Fig. 8
α_r	hot wire resistance coefficient
α_w	angle between hot wire and probe axis
γ	ratio of specific heats ($= 1.4$)
η	recovery ratio
θ	angular coordinate measured from cone axis
θ_l	angle of probe inclination, see Fig. 8
θ_c	cone semi-apex angle
θ_s	outer shock wave angle
μ	viscosity
ξ	non-dimensional distance between body and shock, $\xi = (\tan \theta - \tan \theta_c) / (\tan \theta_s - \tan \theta_c)$
ρ	density
ϕ	azimuthal coordinate measured from the most windward meridian plane
Φ	correlation function for hot wire heat loss

Subscripts

c	condition on cone surface
co	continuum condition
e	equilibrium condition
f	free molecule condition
m	measured quantities
n	needle support condition
o	stagnation condition
r	reference
t	total (temperature, pressure)
v	vortex
w	wire condition
∞	free stream condition

1.0 INTRODUCTION

In the design of present day supersonic aircraft, a pointed cone or a cone-like shape is a common part in the system. It is of great importance to understand and to be able to predict the flow field structure of a supersonic flow past a yawed cone. The calculation of the inviscid flow field around a cone at an angle of attack has occupied the interest of many research workers for the past two decades. From the point of view of inviscid analysis the flow field is conical, there is no length scale and there are only two independent variables, ϕ and θ , see Fig. 1. Since the differential equations are nonlinear and the boundary conditions are not known (at the outer shock) a priori, one has to appeal to numerical methods in order to obtain solutions.

Solutions for slightly yawed cones obtained by Stone (1948, 1952) turned out to require modification at the cone surface. When a cone is exposed to supersonic flow at an angle of attack an elliptical like shock wave is formed and its strength decreases from the far windward side toward the leeward side. Consequently, streamlines entering the disturbed region through the shock at different meridian angles experience different entropy gains. When these streamlines with different entropy converge on the cone surface they form an "entropy layer" (Fig. 2). Ferri (1951) was the first to introduce the concept of the entropy layer where a narrow region near the cone surface sustains a large entropy gradient. Also, he noted that the entropy would be constant on the surface of the cone and multivalued in the plane of symmetry on the surface; this brought about the concept of vortical singularity. Ferri suggested that when the angle of incidence is increased the vortical singularity would "lift off" from the cone surface.

The behavior of the vortical singularity has been studied intensively by Melnik (1966). He showed that for large angles of yaw either the vortical singularity lifts off in the plane of symmetry or it is shifted on the cone surface off the plane of symmetry (Fig. 3). Moretti (1967) also, in his analysis of the flow on the leeward side of a cone, proved that there is a possibility for the vortical singularity to be detached from the cone surface.

Since then quite a few numerical methods have been devised, such as Holt and Ndefo (1970), and the inviscid conical field has been solved. Tables for a wide range of Mach number and for relative incidence α/θ_c less than one are given by Babenko et al. (1966) and by Jones (1969); the latter even solved for α/θ_c slightly larger than unity.

For angles of attack less than the semi apex angle of the cone ($\alpha < \theta_c$) the velocity of the cross flow is less than the local speed of sound, $\sqrt{v^2 + w^2}/a < 1$, which results in elliptic type differential equations. When α/θ_c exceeds one there are regions in the leeward side of the cone where the cross flow Mach number exceeds one and therefore, in this region the governing equations are hyperbolic and the whole region is of mixed type. When this kind of flow exists the cross flow component which is supersonic is slowing down to subsonic toward the most leeward meridian $\phi = 180^\circ$. This leads to the formation of imbedded shocks within the overall disturbed region. The flow is then very difficult to treat theoretically because one does not know a priori the location of the imbedded shock and the location of the cross flow component sonic line.

Bazzhin (1968) tried to solve the problem by using experimental results for assuming the location and the shape of the imbedded shock. His calculations also showed that when the angle of incidence is increased the entropy

distribution can be qualitatively different from the one at small incidence. The constant entropy lines will not then converge and no entropy layer will be formed.

Relatively few experimental investigations of the cone flow field have been made although several measurements on the surface itself, such as pressure and heat transfer, are available [Conti (1961), Guffroy et al. (1968), Holt and Blackie (1956), Julius (1959)]. Tracy (1963) was the first to make extensive measurements of the flow field around a yawed cone and to describe the flow on the leeward side, especially the viscous effects, and he claimed to observe the formation of a single vortex at high angle of incidence. This description of a single vortex has turned out to be erroneous according to later studies, including the present one.

The development of an inviscid theory which will adequately describe the flow field on the leeward side of the cone at high angles of attack is very complicated, not only due to the existence of the mixed region but also due to the important role of viscosity. The only way to learn about this flow is to perform experimental investigations. Because of the rotational character of the flow field and its three dimensional behavior (the entropy varies from one streamline to the other), a survey with a pitot probe alone is not sufficient. These factors make it difficult to survey the flow field and indeed very few people have made experimental studies.

Feldhuhn (1968,1969) investigated the slender cone $\theta_c = 5^\circ$ at hypersonic speeds at very high angles of attack. Rainbird (1968) studied in addition to the external flow the growth and the separation of a turbulent boundary layer on a cone $\theta_c = 12.5^\circ$. George (1969) studied the flow field of a sharp cone $\theta_c = 10^\circ$ at moderate yaw. Most of the available data are in the hypersonic range (except Rainbird $M = 1.8, 4.25$). Besides a pitot

probe Feldhuhn used a five hole cone and an equilibrium temperature probe and Rainbird used a similar cone probe and a Preston surface pitot tube. George used a pitot probe only. All these reports give a similar qualitative picture of the flow field on the leeward side of the cone although there are some differences depending on the angle of attack and way of interpretation of the results.

The purpose of this work is to investigate cone surface conditions experimentally as well as the flow field around the cone at supersonic speeds, with $M_\infty = 2.72$ for various cones ($\theta_c = 10^\circ, 15^\circ, 20^\circ$) at angles of attack up to 30° . A comparison is made with theoretical results for relative incidences $\alpha/\theta_c < 1$. It is hoped that further clarification will be provided about the possible existence of a vortical singularity and its lifting off. The role of viscosity in determining the external flow field will be discussed in order to help to construct an inviscid theory.

2.0 EXPERIMENTAL APPARATUS

2.1 Wind Tunnel

The experiments were carried out in the Aeronautical Sciences Division 6" x 6" supersonic wind tunnel at the University of California in Berkeley. The tunnel is of continuous flow type with an adjustable nozzle which allows a range of Mach numbers of 2.4 to 3.0. Stagnation pressure and stagnation temperature can be varied in the range of $1.3 < p_t < 30$ psia and $50^\circ < T_t < 150^\circ$ F, which allows a variation of the Reynolds number of $1.5 \times 10^5 < Re/ft < 6.6 \times 10^6$. This facility is equipped with a Schlieren and a shadowgraph system which make it possible to observe density gradient regions and to take pictures, and with a multi-manometer board which uses mercury as well as oil. A detailed description of the wind tunnel and its performance is given by Bossel (1967).

2.2 Models and Supports

Three model cones were built in which the semi apex angles of the cones were $\theta_c = 10^\circ, 15^\circ, 20^\circ$. The models were fabricated from brass and polished thoroughly. Pressure taps of 0.030" diameter are around the cones. A sketch of the model showing location of the taps is given in Fig. 4 and the table attached. All the angular sizes are correct within $\pm 0.05^\circ$. Each tap is connected to a copper tube on the base of the cone and from there the pressure is picked up by a plastic tube as shown in Fig. 5.

The models were supported by a hollow arm (through which the pressure tubes passed) disturbing the flow only on the downstream side of the models. An adaptor (Fig. 6) which fixed the cone at an angle of incidence was fitted between the supporting arm and the cone. Seven such adaptors were built in order to set the cones at angles of attack of $0^\circ, 5^\circ, 10^\circ, 15^\circ, 20^\circ, 25^\circ, 30^\circ$ where the accuracy was within $\pm 0.1^\circ$. The pressure

taps were connected to a multi-valve manifold system and the pressure was read on a mercury micromanometer with an accuracy of 0.001" Hg.

2.3 Probe

A special probe was designed and built, as shown in Fig. 7. It consisted of a pitot tube and of a rotating hot wire. The pitot tube was made from a 0.040" O.D. stainless steel tube. The tube was glued with epoxy to a part which housed the hot-wire probe. This part could be rotated in the vertical plane from outside the tunnel by a flexible speedometer cable through a gear of 1:28 ratio. The cable was mounted outside the tunnel to a counter and one could get an inclination of the probe of $\pm 50^\circ$ with an accuracy of 0.5° . The hot wire probe body was built from stainless steel and it could be rotated around its own axis from outside the tunnel by means of another flexible speedometer cable. A ratchet-like device made it possible to fix the probe at eight angular positions within an accuracy of 2° . The wire supports, made of sewing needles 0.022" in diameter, were mounted on the probe body through a teflon part so as to keep them isolated. One support needle was longer than the other so that the wire mounted on the tips formed, instead of a 90° , a 76.6° angle, α_w (measured under a microscope), with the probe axis, Fig. 8.

The wire used was a 0.0002" diameter Wollaston wire (Pt, 10% Rh) and 0.040" long. It was soft soldered, under a microscope, on the tips of the needles.

The mouth of the pitot tube was set a small distance downstream of the hot wire and about 0.040" to one side, so that there would not be any interference between the two.

The pitot probe pressure signal was connected to a Wienco ± 5 psi pressure transducer which was calibrated against the mercury micromanometer.

The electrical signal was recorded on a chart recorder.

The hot wire was connected to a Thermo-System Heat Flux System which maintained the hot wire at a constant resistance (constant temperature). The resistance of the wire could be measured with an accuracy of better than $\pm 0.01 \Omega$ and the wire current could be computed with an accuracy of better than $\pm 5 \times 10^{-5}$ Amp.

3.0 EXPERIMENTAL PROCEDURE AND DATA REDUCTION

3.1 Free Stream Flow Conditions

All the experiments were run under one nominal tunnel condition. The stagnation pressure was set to 8.5 psia which resulted in stagnation pressure of 8.75 psia and with repeatability deviation of less than 1%. The stagnation temperature was set at 70° F and it varied very little during the experiments (within 1° F).

The stagnation pressure was measured at the stagnation chamber of the wind tunnel and the static free stream pressure at the bottom of the test section. Both pressures were measured with the multi mercury manometer.

The Mach number was 2.72, which resulted in free stream Re/ft of 1.66×10^6 . Based on cone height H (see Fig. 3), the Reynolds number was always less than 5.5×10^5 where the boundary layer was assumed to be laminar.

3.2 Model Setting and Alignment

Each cone was aligned at zero angle of attack by means of the supporting arm which could be rotated up to $\pm 5^\circ$. The alignment was achieved when the pressure all around the cone was the same. All the data were then taken and the cone adaptor was changed to set the cone at higher angle of incidence, up to 30° , in increments of 5° . The 20° cone was set only up to 25° because it would vibrate at 30° as a result of introducing blockage into the tunnel.

Because of the limited size of the wind tunnel and the desire to test as large models as possible, careful preliminary tests were made in order to determine the size and position of models needed to avoid interference with tunnel wall boundary layers and reflected shocks.

3.3 Surface Pressure Measurements

In measuring the surface pressure use was made of the symmetry of the flow field about $\phi = 0^\circ, 180^\circ$ planes. Most of the pressure taps were distributed on one side of the cones, namely, from $\phi = 0^\circ$ through $\phi = 180^\circ$. There were a few pressure taps, however, on the other side at $\phi = 202.5^\circ, 225^\circ$, and 270° , by means of which the symmetry was checked. There were also taps at $\phi = 0^\circ, 180^\circ$, and 270° at a closer station to the tip, located at approximately half the distance from the other taps to the cone apex. These taps helped to determine if the flow was really conical. From the taps that were in the region $0^\circ \leq \phi \leq 180^\circ$, those that were in the interval $90^\circ \leq \phi \leq 180^\circ$ were placed at an angle of 11.25° from each other. Due to technical difficulties, the taps at $\phi = 101.25^\circ, 123.75^\circ, 146.25^\circ$, and 168.75° were stationed 0.125" upstream from the others. This should not have caused any problem since the flow was conical anyway.

The surface pressure was measured with the mercury micromanometer where the free stream static pressure p was used as the reference. Because of the time lag, it took about two minutes for each reading. The accuracy, however, was within ± 0.001 " Hg.

In some cases, for example, near the primary and the secondary minima the surface pressure measurements were repeated with very good consistency, thus establishing the reliability of the pressure values at these points.

3.4 Flow Field Survey

The disturbed flow field around the cone was surveyed by the pitot-hot wire probe described earlier. Again the symmetry of the field was utilized and often checked with the pitot tube. The probe was mounted on

an existing traverse mechanism by which the probe could be moved up and down, upstream and downstream and sideways. The position of the probe was indicated by three counters, where the smallest displacement that could be read was 0.001" for the vertical travel, 0.1 mm for the traverse travel, and 0.2 mm for the axial travel.

Since all theoretical results are given in body coordinates, either in polar or reduced coordinates (ξ, η) , all the data in the present work were transformed to these coordinates. The location of the probe was determined by bringing the pitot tip to a known point on the model surface, reading its position on the traverse mechanism counters and then, when in the flow field, recording its relative position to the reference one.

The survey of the flow field was in two parts. One was the detailed study of the flow in the plane of symmetry $\phi = 180^\circ$ where both the pitot and the hot wire were used and the second one, covering the rest of the field, where the pitot probe only was used. In the plane of symmetry, the Mach number M , pitot pressure P_{t_2} , and the total temperature T_t , were determined from the hot wire and the pitot measurements. With the aid of the tables in NACA Report No. 1135 the static pressure and temperature could be computed.

3.4.1 Pitot Survey

The purpose of the pitot tube survey was to determine the location and the shape of the outer shock as well as of the imbedded shock when this exists. The pitot pressure gradient as well as the density gradient that characterized the edge of the vortex determined the size of the lobe of the vortical fluid.

In determining the shock position, the pitot probe was always moved from the disturbed region towards the free stream region. The location of the shock was determined at the mid-way point of the pressure rise.

Although Bannik and Nebbeling (1968) showed that this definition may not be accurate, this procedure was adapted for the present work and agreed very well with observations from the shadowgraph. It is estimated that the error in determining the shock angle θ_s in the θ - ϕ surface is less than 0.2° .

To survey the flow field on the leeward side of the cone, the pitot probe was moved in the transverse direction and using what is essentially Tracy's criterion, i.e., a small jump in the pitot pressure when moving toward the $\phi = 180^\circ$ plane, to determine the existence and location of imbedded shocks. Travelling in the vertical direction also was carried out especially to locate the vortex.

In surveying the flow in the plane of symmetry $\phi = 180^\circ$ the probe was aligned approximately with the flow direction and since the pitot pressure is insensitive to flow direction within $\pm 10^\circ$, no correction was made due to misalignment.

3.4.2 Hot Wire Measurements

The hot wire is capable of providing two thermodynamic properties: 1. the wire recovery temperature when no heat is dissipated in the wire, 2. the heat transfer from the heated wire to the surrounding stream. In addition, the hot wire is sensitive to the flow direction. By using an oblique wire it is possible to determine the velocity direction in a two dimensional flow field.

3.4.2.1 Hot wire data reduction. The heat loss from the hot wire to the surroundings can be expressed in a nondimensional form

$$Nu_m = \frac{i^2 R_w}{(T_{w_m} - T_{e_m}) k_o l \pi}$$

where Nu_m is the Nusselt number, i the electrical current in the wire,

R_w the wire resistance when it is heated, T_{w_m} the measured temperature of the heated wire, T_{e_m} the cold (adiabatic) temperature of the wire when it is not heated, k_o the thermal conductivity of the surroundings at the stagnation condition and ℓ the wire length. (The subscript m stands for "measured").

The temperature T measured by the wire is given by measuring its resistance R and by using the linear relation $T = T_r[1 + \alpha_r(R - R_r)]$ where R_r is the wire resistance at some reference temperature T_r , and α_r is a constant coefficient.

The measured Nusselt number Nu_m is corrected for end losses, since the wire has finite length and is soft soldered at each end to the two needles. The aspect ratio ℓ/d of the wire is of order 200 and the correction may be appreciable. A derivation of this correction is given by Kovaszny (1956) and Dewey (1965). A parameter S is introduced which is

$$S = \frac{d}{\ell} \sqrt{\frac{k_w}{k_o} \frac{R_w}{R_e} \frac{1}{Nu_m}}$$

where d is wire diameter, k_w the thermal conductivity of the wire material and R_e the cold resistance of the wire. Once S is found, it is possible to determine two correction factors C_{Nu} and C_R . Thus the Nusselt number Nu_o and the temperature recovery ratio η for an infinitely long wire are:

$$Nu_o = C_{Nu} Nu_m$$

$$\eta = C_R \eta_m$$

where $\eta = T_e/T_t$; $\eta_m = T_{e_m}/T_t$.

T_t is the total temperature of the surrounding flow. C_{Nu} is a function of S alone and C_R is a function of S and the recovery temperature of

the needle supports. More details are given in the Appendix.

When the measurements are corrected to the case of heat loss from an infinite cylinder (wire), many experimental investigations showed that the Nusselt number is a function of Mach number M and Re_0 , where $Re_0 = \rho U d / \mu_t$, i.e., Reynolds number based on wire diameter and condition behind a normal shock. μ_t is the viscosity at the stagnation temperature. Dewey (1961,1965) has formulated an empirical equation which represents a curve fit of existing experimental data. This formula has the form:

$$Nu_0(Re_0, M) = Nu_0(Re_0, \infty) \Phi(Re_0, M)$$

where $Nu_0(Re_0, \infty)$ represents the dependence of Nu_0 on Re_0 when $M \rightarrow \infty$ and $\Phi(Re_0, M)$ is the departure from this relation when M is finite. These relations are given in the Appendix.

The recovery temperature ratio $\eta (= T_e/T_t)$ is a function of M only in a continuous flow and also a function of Knudsen number Kn_∞ in the transition region, where, as in the present case, the hot wire diameter is of the same order of magnitude as the molecular mean free path (Kn_∞ approximately 0.15). Dewey has proposed an empirical formula which takes into account the effect of free molecule flow on the recovery temperature. The recovery temperature ratio is:

$$\eta = \eta_{co} + \bar{\eta}_*(\eta_f - \eta_{co})$$

where η_{co} and η_f are the values of η at the continuum limit and the free molecule flow limit, respectively, and are functions of M only. The coefficient $\bar{\eta}_*$ is represented as a function of Kn_∞ . The formulas for η_{co} , η_f and $\bar{\eta}_*$ are given in the Appendix.

As one notices from the formulae, the algebraic equations are coupled in such a way that an iteration scheme is required in order to solve for M and T_t . Although the description of the hot wire measurements and data reduction procedure are not yet complete, it would be appropriate at this point to describe the computational scheme which was programmed and computed on the CDC 6400 at the University of California, Berkeley. It runs as follows:

1. Assuming $\eta_m = 1$ the values of T_e , k_o , and Nu_m are computed. S is determined and hence Nu_o . Since Re_o can be expressed as $Re_o = Re_o(M, T_t, P_{t_2})$, using Sutherland's viscosity law, then $Nu_o(Re_o, M)$ can essentially be written as $Nu_o(M, T_t, P_{t_2})$, hence M is found.
2. Kn_∞ is computed, $Kn_\infty = Kn_\infty(M, T_t, P_{t_2})$. Also η_{co} , $\eta_f - \eta_{co}$ and $\bar{\eta}_*$ are determined, and hence η .
3. With the value found for M , the support recovery ratio $\eta_n (= T_n/T_t)$ is computed, and hence the end loss recovery ratio C_R .
4. From the computed C_R and η , one computes η_m , which is then substituted back in step 1.

The iteration converges very rapidly and no significant variation is observed after the third iteration.

3.4.2.2 Determination of the velocity direction. When a hot wire is placed at an oblique angle ($\theta_1 = \alpha_M$ in Fig. 8) to the flow rather than normally, the heat loss of the wire is related to the velocity component which is perpendicular to the wire; the heat loss due to the tangential component is negligible.

The measurements with the hot wire probe were confined to the plane of symmetry $\phi = 180^\circ$ where the flow was two-dimensional, $w = 0$. At each point the hot wire was set at position I (Fig. 8) where the probe

was in the vertical plane $\phi = 180^\circ$ and the output was related to Mn_1 the normal-to-wire component of the Mach number. Then the probe was rotated about its axis at 180° to position II and the output was related to the corresponding Mn_2 . Knowing Mn_1 and Mn_2 , one can then find the velocity direction α_M , which is the angle between the velocity vector and a horizontal line. From the geometry in Fig. 8 it is found that

$$\tan(\theta_1 - \alpha_M) = \frac{Mn_1 - Mn_2}{Mn_1 + Mn_2} \tan \alpha_w$$

where θ_1 is the angle between the probe axis and the horizontal line. If one writes:

$$A = \theta_1 - \alpha_M$$

then

$$M = \frac{Mn_1}{\sin(\alpha_w + A)}$$

Knowing M and α_M and the position of the probe relative to the cone, it is possible to find the cross flow (in the direction of θ) Mach number M_θ . With this method M and M_θ can be determined within an accuracy of about 7%.

3.4.2.3 Hot wire experimental procedure. Each wire, mounted on the support needles, was annealed to a dull glow for several minutes and brought back to room temperature before calibration. This was done in order to avoid great changes in the electrical resistivity coefficient after each heating. The wire was then calibrated in water and the relation $T = T_r[1 + \alpha_r(R - R_r)]$ was established. Since the range of temperature was small, no second order correction was needed for determining T ; α_r was a constant independent of temperature. The manufacturer's data for the wire

were taken for granted, i.e., wire diameter 0.0002" and its resistance per foot at 20° C 2760 Ω /ft. This last figure was used to compute the wire length.

The probe was aligned in the free stream flow so that the $\theta_1 = 0^\circ$ position was achieved by rotating the probe about its axis and verifying that the hot wire output is the same for each angular position (the angle between the free stream velocity vector and the wire should not change while the probe is rotated). The probe was then brought into the disturbed region in the plane of symmetry $\phi = 180^\circ$. Then, by means of the flexible cable and its gear it was positioned approximately parallel to the cone wall and its exact inclination θ_1 was determined by the counter.

At each point the cold resistance was measured, i.e., the wire resistance when it was not heated. Then the wire was heated using an excess heat ratio $(R_w - R_e)/R_e$ of 23% in order to get good sensitivity to velocity direction. By measuring the wire voltage output and R_e , the temperature T_{em} and the measured Nusselt number could be computed. This procedure was repeated twice at each point for positions I and II of the wire (see Fig. 8).

3.4.3 Flow Visualization

In order to get a better understanding of the flow field it was desirable to use some flow visualization techniques; no quantitative studies were made apart from some rough estimates, and the results obtained were mostly qualitative.

Three methods were used:

1. Schlieren System. The Schlieren system was used in the usual manner. The light that passed the test section was perpendicular to the

$\phi = 0^\circ$, $\phi = 180^\circ$ plane. Colored Schlieren pictures could be taken with a Polaroid camera, Fig. 9.

2. Vapor Screen Technique. For high angles of attack the vapor screen technique was used to visualize the flow field. This was done by adding water to the wind tunnel through the diffusion part and when sufficient water was added to the air, condensation would occur in the test section. Using the point source light of the Schlieren system, one of its parabolic mirrors and a black dark paper with a slit cut in it, all the light was blocked out except for a narrow beam that passed through the slit and the region of interest in the test section. Regions with high density would appear bright and those with low density -dark. Thus shock surfaces and vortices were visible.

3. Surface Oil Flow. In order to visualize skin friction lines and detect possible separation, it is common to spread the model surface with oil and observe its flow. In the present investigation the oil was introduced from outside the tunnel through the front pressure taps on the model. The oil was heavy (SAE 50) and was colored with lamp black.

4.0 RESULTS AND DISCUSSION

The reduced experimental data will now be discussed. Since there are no theoretical results for relative incidences $\alpha/\theta_c > 1$, no comparison can be made, which makes it harder to analyze the results. For the $\alpha/\theta_c < 1$ range there are no theoretical calculations for the present Mach number, $M = 2.72$. However, a comparison with Jones' (1969) tables is made for this range. A linear interpolation has been used to obtain his results for $M = 2.72$.

The present experimental results are also compared with other experimental data, but since those results were obtained under different flow conditions, the comparison is of a qualitative nature only.

Before going into details, it is worthwhile firstly to describe in general what happens to the flow field about a yawed cone. When the angle of attack is increased the encircling shock gets stronger on the windward side of the cone and weaker on the leeward side. For moderate yaw angles $\alpha/\theta_c \approx 1$ the boundary layer may separate on the leeward side, but the separation region is very thin--it is washed out by the main stream and does not affect the outer inviscid flow. For higher angles of attack, imbedded shocks are likely to form and the separated boundary layer builds itself into a lobe of vortical fluid of significant size. In fact, two such symmetrical lobes are formed on the leeward side of the cone.

A remark about three dimensional boundary layer separation.

The concept of boundary layer separation is used in a three dimensional boundary layer on a cone by analogy with two dimensional separation. It should be noted, however, that no real separation occurs and the skin friction does not vanish at the point (in fact, a line) of separation; only its component in the circumferential direction ϕ vanishes.

4.1 Surface Pressure Distribution

The surface pressure distributions for all the cones that were investigated are shown in Figs. 11a-e, where the pressure coefficient is

$$C_p = \frac{p_c - p_\infty}{\frac{1}{2} \rho_\infty U_\infty^2}$$

As the angle of attack is increased the pressure on the windward side rises very rapidly and decreases moderately on the leeward side. When the yaw is small, i.e., the relative incidence is small $\alpha/\theta_c < 0.5$, $dp_c/d\phi$ is negative throughout, the minimum pressure occurs on the most leeward meridian $\phi = 180^\circ$ and there is no boundary layer separation of the cross flow. As the relative incidence is further increased, the minimum pressure point is shifted off the $\phi = 180^\circ$ line; this first happens when $d^2p_c/d\phi^2 = 0$ at the $\phi = 180^\circ$ line. The minimum is then rapidly shifted to about $\phi = 135^\circ$. Although the pressure gradient becomes adverse, the pressure does not change very much in the leeward region.

The pressure coefficient agrees quite well with Jones' results for $\alpha/\theta_c < 1$. The slightly higher pressure found on the windward side can be attributed to viscosity where the boundary layer thickness actually increases the effective cone angle θ_c . The small deviation in the leeward region may also be due to viscous effects, but since the disagreement is not systematic, it is impossible to pin-point the cause exactly.

At larger angles of attack $\alpha/\theta_c > 1$, the minimum pressure point moves slightly further towards the windward side to around $\phi = 125^\circ$. At that point it seems that increasing the relative incidence does not significantly affect the location of the pressure minimum, at least as it is observed for the 10° and 15° cones. The pressure coefficient becomes

negative for $\phi > 100^\circ$ and a plateau region of almost constant pressure is observed approximately at $135^\circ < \phi < 170^\circ$. There most of the separated vortical fluid can be found. It is worthwhile noting that this plateau is similar to that which appears at the separated bubble in the two dimensional supersonic flow around a compression corner.

For relative incidences $\alpha/\theta_c > 2$, the two vortices that are formed from the rolling up of the separated flow are quite distinct. In the region $170^\circ < \phi < 180^\circ$ the adverse pressure gradient is pronounced, which causes a strong boundary layer out-flow from the most leeward generator.

Rainbird (1968a,b) has observed for $\alpha/\theta_c > 2$ that a second pressure minimum is at $\phi = 166^\circ$. Since in the present investigation the surface pressure has not been recorded continuously with ϕ but rather at a discrete number of stations, it is difficult to locate this minimum very accurately. It can be seen, however, from Figs. 11a,d that there exists a second pressure minimum around $\phi = 170^\circ$, for $\theta_c = 10^\circ, 15^\circ, \alpha = 25^\circ, 30^\circ$.

Rainbird measured the surface pressure coefficient for a 5° cone at relative incidences of 2.1 and 2.5 and for M_∞ of 1.79 and 4.25. His circumferential pressure distribution differs considerably in the qualitative sense from the present one, by the fact that his two minimum pressure points are very distinct and low, followed by a rather large positive pressure gradient compared to the quite flat minimum observed here. As has been pointed out by Rainbird, the existence of an imbedded shock might give a sharp rise to the pressure following the first minimum. This has not been observed and indeed, as will be noted later, the imbedded shock turns out to be weak.

As previously mentioned, the surface pressure was measured at some stations which were closer to the cone apex. If there were some dependency of the pressure on viscosity, i.e., on Reynolds number, it would show up in different pressure readings at two taps on the same generator. The Reynolds number Re_x based on the distance from one tap to the cone apex was approximately twice as large as the Re_x of the other. In particular, for the most leeward generator $\phi = 180^\circ$ for high relative incidence one would expect a strong viscous effect and therefore, a strong dependency on Re_x . Indeed, as observed by Feldhuhn et al. (1968, 1969), there is a significant pressure decrease along the $\phi = 180^\circ$ generator, which means that the pressure is reduced when Re_x is increased. In the present investigation no significant difference in the pressure was observed. This only verified the assumption about the conical nature of the flow field.

4.2 Oil Flow

The streamline pattern on the cone could be seen very well with oil (Fig. 10). For high angles of attack, a streamline originating on the windward side of the cone would extend around the cone to the leeward side up to the separation line. From the angle the streamline made with the cone generators one could see that in certain regions the cross flow velocity was of the same order as the radial one. The streamlines would turn sharply toward the separation line where oil accumulation was observed. The separation line coincided with a cone generator. Thus the separation phenomenon, although undoubtedly associated with viscosity, has a conical behavior.

The separation line would always occur close (within 5°) to the primary pressure minimum. This agrees very well with the fact that a compressible boundary layer would separate immediately when it is under adverse

pressure gradient. For large relative incidence, the flow of the boundary layer away from the most leeward meridian, could be observed. The secondary separation could not be seen, but this could be due to the unevenness of the oil spread on the model surface.

4.3 Static Forces

From the measured surface pressure the axial force C_A and the normal force C_N coefficients were computed, where

$$C_A = \frac{1}{\pi} \int_0^{\pi} C_p d\phi$$

and

$$C_N = \frac{\cot \theta_c}{\pi} \int_0^{\pi} C_p \cos \phi d\phi$$

The integrals were approximated by the trapezoidal rule.

The axial force coefficient is plotted in Fig. 12, and is compared with Jones' computations for $\alpha/\theta_c \leq 1$. For relative incidence up to unity, the axial force does not vary much as the angle of attack is increased. For $\alpha/\theta_c > 1$ it becomes increasingly large and even more so when the cone angle θ_c is larger. The agreement with Jones' results is quite good, considering the experimental errors and approximate integration.

The normal coefficient is shown in Fig. 13. For the present range of model inclination, C_N is growing in a rather linear fashion with the relative incidence. The slopes of the normal coefficient $(\partial C_N / \partial \alpha)_{\alpha=0}$ based on Sims (1964) are shown also. For the 10° cone the measured C_N is higher than the Sims slope would indicate. For the other cones the agreement is very good.

The drag coefficient is

$$C_D = C_N \sin \alpha + C_A \cos \alpha$$

and is shown in Fig. 14. Due to the increasing viscous effect for large yaw, represented by C_D , the drag coefficient is increasingly large when the angle of attack is increased.

The lift coefficient is

$$C_L = C_N \cos \alpha - C_A \sin \alpha$$

and is shown in Fig. 15. There is not much difference between the C_L for the various cones. The lift coefficient grows in a rather linear fashion but it will probably level off for very large yaw and even go down, as noted in Feldhuhn and Pasiuk (1968).

To complete this part, the lift to drag ratio C_L/C_D is plotted in Fig. 16. Maximum values of C_L/C_D are achieved at relative incidence of approximately 1 for the 15° and 20° cones and of approximately 1.5 for the 10° cone. It is also seen that the slenderer the cone the higher is the C_L/C_D ratio achieved.

4.4 Outer Shock Wave

The shape of the outer shock which separates the free stream from the disturbed region is shown in Figs. 17a-e. The results are plotted on the spherical $\phi - \theta$ surface. Again a comparison is made with Jones' results where it is seen that in general there is good agreement regarding the shock shape and often the θ_s of the experiment is slightly higher than that of the theory. This is due to the viscous effect of the boundary layer.

The outer shock on the leeward side of the cone is very weak and cannot be seen by means of the Schlieren system. However, the signal from the pitot tube, when passing through the shock wave, although small, was quite distinct. A pitot signal (and a hot wire signal as well) could be observed on the leeward side even for the large incidences. The θ of a

Mach wave for $\alpha/\theta_c > 1$ ($\theta_{MW} = \alpha + 21.57^\circ$) fell short of the observed θ_s at $\phi = 180^\circ$ by one to three degrees. The difference grew with the angle of attack because then, the effect of the displaced vortices was larger. It is widely thought that for large yaw the outer shock degenerates into a Mach cone on the leeward side. This will not happen immediately when α exceeds θ_c but for some α greater than θ_c . Indeed the shock strength, although observable, is practically zero in terms of $\Delta p_t/p_{t_\infty}$, and the apex of the Mach cone is shifted due to viscous effects.

In Bazzhin (1970) it is found from shock wave computations that there can be another possibility. That is to say, for thicker cones or greater Mach number the shock wave intensity may be non-zero all along its length. This result is still to be verified experimentally, and this presents a problem, because it is difficult to distinguish between a Mach wave signal, the effect of bluntness of even a very sharp cone and a very weak shock.

4.5 Imbedded Shocks

The internal or the imbedded shocks are so called because they are formed within the disturbed region between the outer shock and the cone surface. The location of the internal shocks as determined by the pitot tube is shown in Figs. 18a-e. As is expected, the imbedded shocks start to appear when the angle of attack exceeds the cone angle. The shock is then very weak and very short. The imbedded shock appears near the separation point. It is as yet undetermined if the imbedded shock results from an interaction between a compressible inviscid flow with the boundary layer, or just from the inviscid flow where the flow must be turned through a shock. It is probably a consequence of both requirements.

The imbedded shock is not actually observed until $\alpha/\theta_c > 1.3$,

and for the 20° cone, $\alpha = 25^\circ$, it is not detected at all. If the shock exists at this moderate yaw, it is very weak and very short and is swallowed up by the boundary layer. This agrees with the experimental results of George (1969) and Tracy (1963) for hypersonic flow.

At higher incidence the strength of the internal shock as well as its length grow. There appears a second and weaker branch of the imbedded shock, which points toward the symmetry plane $\phi = 180^\circ$. The appearance of a second branch is to be expected for larger yaw, since one shock will not be sufficient to turn the flow so that $w = 0$ condition will be attained at the plane of symmetry. This was also observed by Feldhuhn (1969) and Tracy (1963).

The strength of the internal shock (i.e., the pitot probe signal) is rather weak and decreases when moving away from the surface of the cone until it disappears. Thus, not a very sharp pressure increase would be expected on the cone surface, as indeed has been observed. Because of their weakness the imbedded shocks could neither be seen with the Schlieren system nor detected by the vapor screen technique.

4.6 The Viscous Layer and the Vortex System

In employing inviscid theories to solve the flow field around the cone, it is important to know how thick the boundary layer is in order to estimate the accuracy of the theory when boundary layer thickness is ignored. For small yaw the viscous layer is very thin, within the order of the probe size; it is not measurable with the present probe and can be ignored. For larger yaw, because of the increasingly adverse pressure gradient on the leeward side of the cone, the boundary layer is thickening and separates there. The separation region stays thin for $\alpha/\theta_c < 1$. The boundary layer on the windward side ($\phi < 100^\circ$) remains thin even for very high incidence.

The two separated shear layers would roll into two symmetrical lobes of vortical fluid. As is shown in Figs. 18 and 19, the size of the vortex is increasing with the angle of attack.

The outer boundary of the vortices has been observed very clearly for high incidence with the Schlieren system (Fig. 9). The whole vortex system was made visible by the vapor screen technique. The density of the flow inside the vortex system is much smaller than in the surrounding fluid. The vortex flow appears as a dark region in the vapor screen while the surrounding flow is bright; the boundary between the vortical fluid and the outer flow is very distinct.

Before proceeding further, it is worth noting that although the formation of the vortex system is due to viscosity, once it is formed, the role of viscosity in the vortex system is important only at its boundary. The dissipation of energy due to viscosity will take place in the very thin shear layer which surrounds the vortical fluid. However, when dealing with the overall effect of viscosity on the outer flow, the size of the vortex system (sometimes called viscous hump) is the characteristic viscous length which one has to compare to the local body dimension in order to decide whether it is important or not.

The relation between the maximum vortex height, expressed in terms of the angle θ_v , and the cone angle θ_c is given in Fig. 19a as a function of the relative incidence. It is seen that θ_v/θ_c grows almost linearly with α/θ_c . In Fig. 19b the same data are shown in terms of the reduced coordinate $\xi_v = (\tan \theta_v - \tan \theta_c)/(\tan \theta_s - \tan \theta_c)$. It is seen that ξ_v is nearly a constant in the range of α/θ_c between one and three.

In Figs. 18a-e the outer boundary of the viscous layer is shown. At this boundary there exists a large pitot pressure gradient; the pitot

signal drops when moving from the outer flow towards the cone surface. Since the same pitot pressure behavior is found when entering the vortical flow, no distinction is made between the outer shear layer and the outer boundary of the vortex. In fact, for moderate yaw the vortical field is swallowed altogether into the boundary layer. Thus as far as the outer flow is concerned, the region between the outer layer and the cone surface is a region where the viscous forces are important. One sees clearly that this region grows with angle of attack but for $\alpha/\theta_c < 1$ it is quite thin.

These results differ from those discussed by George (1969) and Tracy (1963), where for hypersonic flow quite a large viscous region was observed for smaller relative incidences.

Although the role of viscosity is important in the boundary layer separation as well as in the formation of the vortices, one obtains similar flow structure for higher Reynolds number ($Re_L = 6.8 \times 10^7$, (Rainbird, 1968b)). It is noticed also that as the distance x from the cone apex increases, the value of Re_x is increased but the flow field structure maintains its conical behavior. However, as shown in Feldhuhn (1969), the surface pressure might be dependent on Re_x . It has also been observed by Rainbird that for large yaw $\alpha/\theta_c > 3.1$ the two vortices formed on the leeward side of the cone are not so stable and do not keep their symmetrical appearance.

4.7 The Leeward Meridian Plane $\phi = 180^\circ$

4.7.1 The Vortical Singularity

The vortical singularity mentioned in the Introduction is first discussed from a theoretical point of view. This singularity is a point on the $\phi - \theta$ surface which, for moderate yaw ($\alpha/\theta_c < 1$), lies on the cone surface at $\phi = 180^\circ$. For higher angles of attack it is shown in Melnik (1966) and Moretti (1967) that this point may lift off the surface

to some point in the plane of symmetry $\phi = 180^\circ$.

From the inviscid standpoint the vortical singularity is characterized by the following properties:

1. It lies in the plane of symmetry $\phi = 180^\circ$.
2. The different constant entropy streamlines in the neighborhood of the singularity are pointing toward it and meet there. Therefore the entropy is multivalued at this point.
3. Consequently, the stagnation pressure as well as the radial velocity u are multivalued, but the static pressure is single valued (Holt, 1954).
4. The singular point is a "stagnation" point in the $\phi - \theta$ surface, which means that the velocity there is directed along the radial line and v and w are zero.

In reality singular points do not exist. The multivalued stagnation pressure at the vortical singularity will tend to be smeared out by viscous effects over some finite, though small, distance. For moderate yaw when the singular point lies on the cone surface or very close to it, there will exist an entropy gradient due to the viscous boundary layer. Thus if any other gradient exists as a result of an inviscid theory, it will be swallowed by the boundary layer and there is no way it can be detected experimentally and identified as such.

Even for large angles of yaw when the singularity is supposed to be somewhere above the cone, it is still difficult to detect the singular point only by observing large stagnation pressure gradients. This is because of the existence of large gradients due to the vortices. Thus, if one tries to locate, within experimental limits, the vortical singularity some other or additional criteria should be taken into account such as $v = 0$.

In his experiments $M_\infty = 5$, $\alpha/\theta_c = 4.8$, Feldhuhn (1969) found the singular point for which $v = 0$ to be very far ($\alpha/\theta_c \approx 4.5$) from the cone surface. Another attempt to prove experimentally the existence of the vortical singularity was made by George (1969). He did this with the aid of a pitot probe only and by assuming constant static pressure within the viscous layer. This enabled him to locate the small region of a steep stagnation pressure gradient and to assign the singular point to this region. At his flow condition ($M_\infty = 7.35$, $\alpha/\theta_c = 0.8, 1.2$) the singular point was found approximately, on the edge of the viscous hump.

Before proceeding further, one must bear in mind that the experiments just referred to were carried out in hypersonic flow under different free stream conditions. The same relative incidences also do not guarantee good comparison because the thickness of the cone (θ_c) is by itself important. Nevertheless, it is worthwhile to compare the results qualitatively.

In the present investigation the main criteria used to establish the location of the vortical singularity is that $v = 0$ or $M_\theta = 0$, Fig. 20. However, this by itself is not sufficient, because by the time a vortical-singularity-like stagnation point is formed, another stagnation point off the cone surface is formed also, in the plane of symmetry. This is due to the formation of two recirculation regions (vortices). This last stagnation point is a near-wake-like stagnation point and the streamlines at the plane of symmetry are pointing away from the point. At the same time, of course, there is a stagnation point on the cone surface itself.

Up to relative incidences of 1.5 no stagnation point is found off the cone surface. Rainbird (1968a,b) estimates the relative incidence at which the vortical singularity lifts off by $2(\alpha/\theta_c)_a$, where $(\alpha/\theta_c)_a$ is

the minimum relative incidence for separation. At higher yaw the recirculation regions build up, and also, one would expect a "lift off" to occur. There will be two stagnation points where the vortical singularity has to be above (in the $\phi - \theta$ surface) the near-wake-like stagnation point. It is seen in Figs. 20 a-c that there is a small region where M_θ is about zero. In this range, the two stagnation points are very close to each other and within the present experimental measurements cannot be distinguished.

At still higher angles of attack a rather more pronounced distinction seems to exist between the two points, where M_θ is clearly positive in that region. Note that M_θ is in the direction of θ and is negative in most of the flow field. There is an indication that the distance between the two stagnation points will grow when the angle of incidence is increased.

It can be seen from Figs. 21a-c that the vortical singularity point lies in a region of high stagnation pressure gradient which corresponds to large entropy gradient. But since this point is very close to the viscous region and the measurements are by no means that accurate, this pressure gradient may be due to viscous dissipation as well. As long as the singularity lies close to the viscous hump, some of the total pressure drop is probably due to viscosity. Considering, however, the above discussion concerning the behavior of M_θ , it is believed that part of it is due to the existence of the vortical singularity.

4.7.2 The Flow Field in the Plane of Symmetry $\phi = 180^\circ$

Before going into a detailed discussion of the results, it should be noted that the probe used in the survey is by no means a boundary layer probe. Thus, there was a significant probe-wall interaction when the

probe was brought very close to the cone surface. It was estimated that this effect was dominant in the range $\theta_c < \theta < \theta_c + 1^\circ$,

In addition to the M_θ graphs already discussed above, the distributions of stagnation pressure shown in Fig. 21, static pressure shown in Fig. 22 and static temperature in Fig. 23 in the plane of symmetry $\phi = 180^\circ$ are plotted. Since stagnation temperature variation throughout the flow field was less than 1% and equal to the free stream T_t , there was no real significance in plotting it.

For relative incidences up to one, the stagnation pressure is almost constant throughout the plane apart, of course, from the still thin viscous boundary layer. The flow in the plane of symmetry can be regarded then as essentially isentropic. In the static pressure distribution there is a general good agreement between Jones' calculations and the experiments. The experimental results seem to have a more level pressure distribution. The static temperature in the theory as well as in this experiment changes very little in the plane of symmetry. The theory shows a high temperature gradient very close to the wall. This could not be picked up by the present investigation.

When the relative incidence is increased a stagnation pressure gradient starts to build up. The region of lower total pressure is spreading out as the angle of attack is increased. This pressure gradient is, as discussed above, associated with the existence of the entropy singularity and the viscous hump. Above the vortical singularity point the stagnation pressure is practically the same as its free stream value. It should be noted that stagnation pressure jump across the outer shock in the neighborhood of the $\phi = 180^\circ$ plane is practically zero even if a more pronounced static pressure jump prevails.

The static pressure drops rather smoothly at high angles of attack. The flow experiences an isentropic expansion over part of the plane. It is noticed that close to the wall the pressure is nearly a constant.

The static temperature is dropping down where the flow expands. The appearance of the viscous hump, however, tends to increase the temperature and eventually, near the wall, the temperature rises quite sharply.

In surveying the flow in the plane of symmetry and making comparison with Feldhuhn (1969), an important difference has been observed with regard to the flow field structure. It has been observed there, with the Schlieren system as well as with the pitot tube, that for high angle of attack, two regions of high density gradient exist in the plane of symmetry, whereas in the present investigation only one such region could be detected. Since in Feldhuhn (1969) the free stream conditions were different ($M = 5$) as well as the cone thickness (5°), it is believed that as far as the inviscid field is concerned the flow field structure depends on free stream conditions and on the cone angle as well as on the relative incidence.

5.0 CONCLUSIONS AND SUGGESTIONS

An experimental study of the flow field on and around sharp yawed cones has been conducted with free stream Mach number of 2.72 and Reynolds number 1.66×10^6 Re/ft. The following conclusions have been reached:

1. For a relative incidence α/θ_c up to one, there is a very good agreement between the (Jones) theoretical results and the experimental ones. The boundary layer is thin and although separation takes place on the leeward side of the cone around $\alpha/\theta_c = 0.8$ the separation region stays very thin and close to the wall; thus, the viscous effect can be ignored (at least to the first order) in the inviscid calculations.

2. As the relative incidence is increased $\alpha/\theta_c > 1.3$ imbedded shocks are formed. The strength of those shocks is very weak. The separation line moves upstream, in the direction of decreasing ϕ , with the increasing angle of attack. The two symmetrical separated shear layers roll up into two symmetrical lobes of vortical fluid.

3. For still higher angle of attack $\alpha/\theta_c > 2$, a second pressure minimum is observed which indicates the existence of a secondary separation flow on the leeward side of the cone. The primary separation line moves very little or not at all upstream toward the windward side when the angle of incidence is increased. The angular extent of the vortices increases significantly but still maintains its conical behavior. The size of the imbedded shock increases also, and a second branch is developed. A proposed flow field structure is shown in Fig. 24.

4. At this large yaw the viscosity effect can no longer be ignored. On the leeward side of the cone the viscous layer interacts sharply with the inviscid flow field and together with the vortices modifies significantly the inviscid flow. Account of these effects can be taken while

constructing an inviscid theory, by introducing a vortex sheet and modifying the cone shape on its leeward side.

5. The outer shock wave neither vanishes completely nor degenerates into a Mach cone on the leeward side of the cone, even for large yaw. Its strength, however, is very small, and its location is probably very much affected by the viscous hump.

6. The vortical singularity point can be determined experimentally, when it is not on the cone surface. It lifts off the wall and can be detected when the relative incidence is about 1.5. Because of the nearness of the vortical singularity to the near-wake-like stagnation point, it is impossible to detect a "lift off", if any, at a smaller angle of attack.

Further investigations and suggestions. Since different investigations resulted in different flow field structures at different free stream conditions, it seems that a comprehensive experimental study should be made for various cone thicknesses, for relative incidences of one to a very large yaw, and for a wide range of Mach numbers.

Still more work is to be done to develop a good, reliable and small probe to measure a three dimensional flow in order to survey the whole flow field and to investigate the vortex system.

Since the flow field structure on the leeward side of the cone is quite complicated and changes over small distances, it is suggested that flow field as well as the cone surface measurements should be taken in a continuous manner and not just at a discrete number of points.

REFERENCES

- Ames Research Staff (1953), "Equations, Tables, and Charts for Compressible Flow," NACA Report No. 1135.
- Babenko, K. I., et al. (1966), "Three-Dimensional Flow of Ideal Gas Past Smooth Bodies," NASA TT F-380.
- Bannink, W. J. and Nebbeling, C. (1968), "Determination of the Position of a Shock Wave from Pitot Tube Experiments," Technological University of Delft (Department of Aeronautical Engineering), Delft, The Netherlands, Report VTH-147.
- Bazzhin, A. P., Trusova, O. N. and Chelysheva, I. F. (1968), "Calculation of Flow of a Perfect Gas Past Elliptic Cones at Large Angles of Attack," Izv. An. SSSR M. Zh. G. No. 4.
- Bazzhin, A. P. (1971), "Some New Features of Conical Flows Around Cones at Large Angles of Incidence," in Lecture Notes in Physics No. 8, Springer-Verlag.
- Bossel, H. (1967), "Flow Studies and Turbulence Measurements in the Hesse 6-inch Supersonic Wind Tunnel," University of California, Berkeley Aeronautical Sciences Report AS-67-2.
- Conti, R. J. (1961), "Laminar Heat Transfer and Pressure Measurements at a Mach Number of 6 on Sharp and Blunt 15° Half-Angle Cones at Angles of Attack up to 90°," NASA TN D-962.
- Dewey, C. F., Jr. (1961), "Hot Wire Measurements in Low Reynolds Number Hypersonic Flows," ARS J. 12, 1709-1717.
- Dewey, C. F., Jr. (1965), "A Correlation of Convective Heat Transfer and Recovery Temperature Data for Cylinders in Compressible Flow," J. Heat & Mass Transfer 8, 245-252.

- Feldhuhn, R. H. and Pasiuk, J. (1968), "An Experimental Investigation of the Aerodynamic Characteristics of Slender Hypersonic Vehicles at High Angles of Attack," U. S. Naval Ordnance Laboratory, White Oak, Maryland, NOLTR 68-52.
- Feldhuhn, R. H. and Winkelmann, A. E. (1969), "Separated Flow Phenomena on a Slender Cone at Mach 5," U. S. Naval Ordnance Laboratory, White Oak, Maryland, NOLTR 69-36.
- Feldhuhn, R. H. (1969), "An Experimental Investigation of the Flow Field Around a Yawed Cone," U.S. Naval Ordnance Laboratory, White Oak, Maryland, NOLTR 69-187.
- Ferri, A. (1951), "Supersonic Flow Around Circular Cones at Angles of Attack," NACA TR 1045.
- George, L. O., Jr. (1969), "An Experimental Investigation of the Flow Field Around an Inclined Sharp Cone in Hypersonic Flow," Sandia Laboratories, Albuquerque, New Mexico, SC-RR-69-577.
- Guffroy, D., Roux, B., Marcillat, J., Brun, R. and Valensi, J. (1968), "Étude Théorique et Expérimentale de la Couche Limite autour d'un Circulaire Place en Incidence dans un Courant Hypersonique," AGARD Conference Proceedings No. 30, Hypersonic Boundary Layers and Flow Fields, Paper #20.
- Holt, M. (1954), "A Vortical Singularity in Conical Flow," Quart. J. Mech. and Appl. Math. 7, 4, 438-445.
- Holt, M. and Blackie, J. (1956), "Experiments on Circular Cones at Yaw in Supersonic Flow," J. Aero. Sci. 23, 10, 931-936.
- Holt, M. and Ndefo, E. (1970), "A Numerical Method for Calculating Steady Unsymmetrical Supersonic Flow Past Cones," J. of Computational Physics 5, 3, 463-486.

- Jones, D. J. (1969), "Tables of Inviscid Supersonic Flow About Circular Cones at Incidence $\gamma = 1.4$," AGARDograph 137, Part 1 and Part 11.
- Julius, J. (1959), "Measurements of Pressure and Local Heat-Transfer on a 20° Cone at Angle of Attack up to 20° at a Mach Number of 4.95," NASA TN D-179.
- Kovasznay, L. S. G. (1954), "Hot Wire Method," in Physical Measurements in Gas Dynamics and Combustion, High Speed Aerodynamics and Jet Propulsion, Princeton Series, Vol. 9, Princeton University Press, Princeton, N. J., pp. 319-241.
- Melnik, R. E. (1966), "Vortical Singularities in Conical Flows," Grumman Aircraft Engineering Corp., RE-251J. Also, AIAA J. 5, 4, 631.
- Moretti, G. (1967), "Analysis of Conical Flow on the Leeward Side of a Cone at Angle of Attack," General Applied Science Laboratories, Inc., Westbury, N. Y., Technical Report No. 673.
- Rainbird, W. J. (1968a), "The External Flow Field About Yawed Circular Cones," AGARD Conference Proceedings No. 30, Hypersonic Boundary Layers and Flow Fields, Paper #30.
- Rainbird, W. J. (1968b), "Turbulent Boundary Layer Growth and Separation on a Yawed Cone," AIAA J. 6, 12.
- Schlichting, H. (1968), Boundary Layer Theory, Sixth Edition, McGraw Hill Book Co., N. Y., pp. 317-319.
- Sims, J. L. (1964), "Tables of Supersonic Flow Around Circular Cones at Small Angle of Attack," NASA SP-3000.
- Stone, A. H. (1948), "On Supersonic Flow Around a Slightly Yawing Cone, Part 1," J. Math. and Phys. 27, 67-81.
- Stone, A. H. (1952), "On Supersonic Flow Around a Slightly Yawing Cone, Part 11," J. Math. and Phys. 30, 200-213.

Tracy, R. R. (1963), "Hypersonic Flow Over a Yawed Circular Cone," Graduate Aeronautical Laboratories, California Institute of Technology, Pasadena, Calif., Memorandum No. 69.

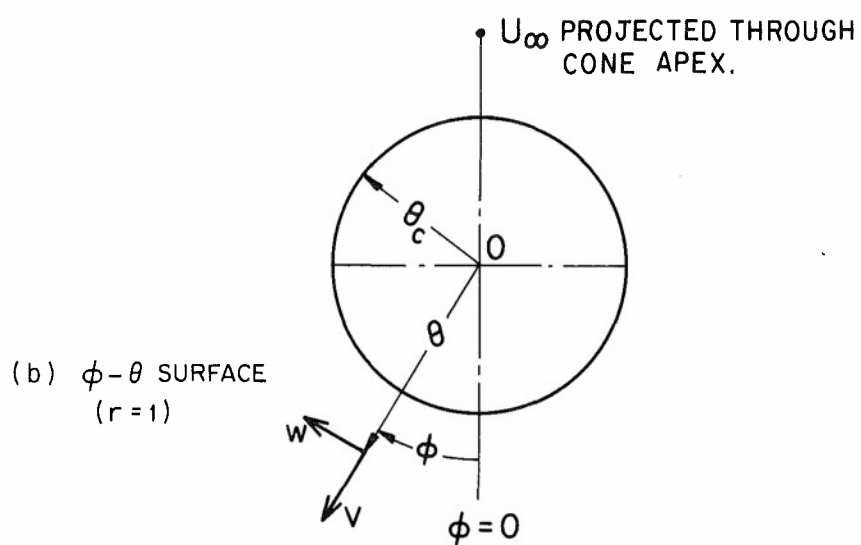
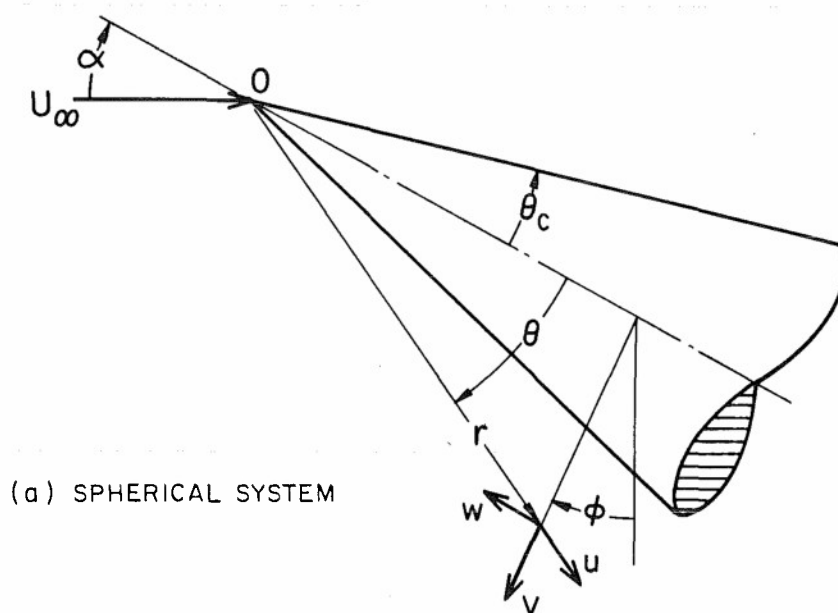


FIG. 1 COORDINATE SYSTEM AND VELOCITY COMPONENTS

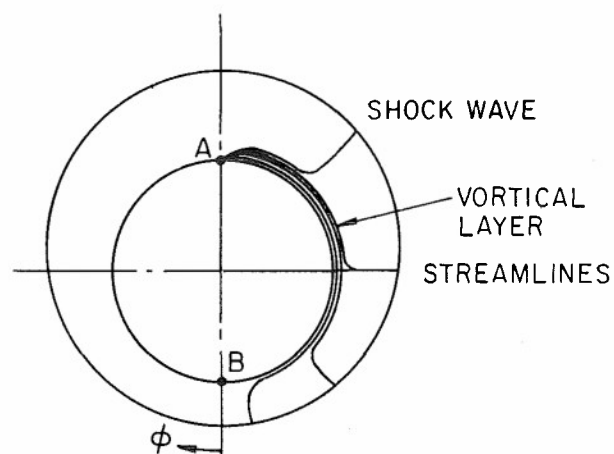
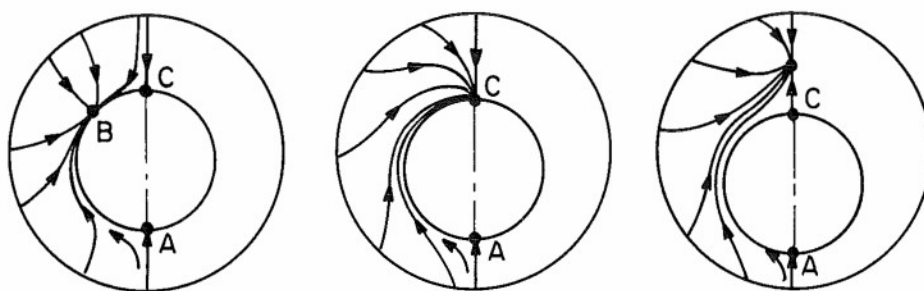
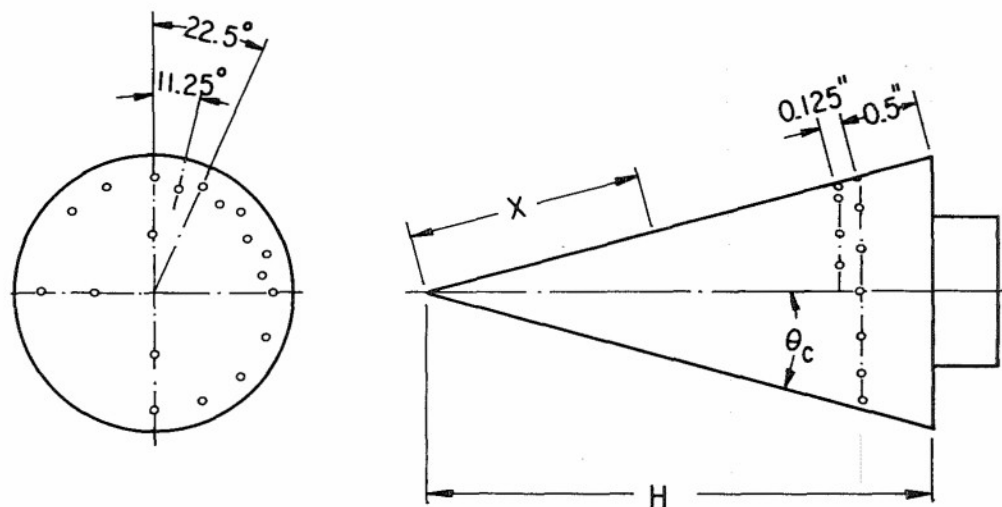


FIG. 2 VORTICAL LAYER ON AN INCLINED CONE
(FROM FERRI, 1950)



(a) 3 STAGNATION POINTS (b) 2 STAGNATION PTS. (c) 2 STAGNATION PTS.

FIG. 3 STREAMLINE PATTERN ON A CIRCULAR CONE
AT MODERATE TO LARGE ANGLES OF ATTACK
(FROM R.E. MELNIK, 1966)



θ_c	10°	15°	20°
H	4"	3.25"	2.5"
X	2.125"	1.5"	1.0"
Re_H	5.57×10^5	4.52×10^5	3.48×10^5

$$Re_H = \frac{U_\infty H}{\nu_\infty}$$

FIG. 4 MODEL AND PRESSURE TAPS

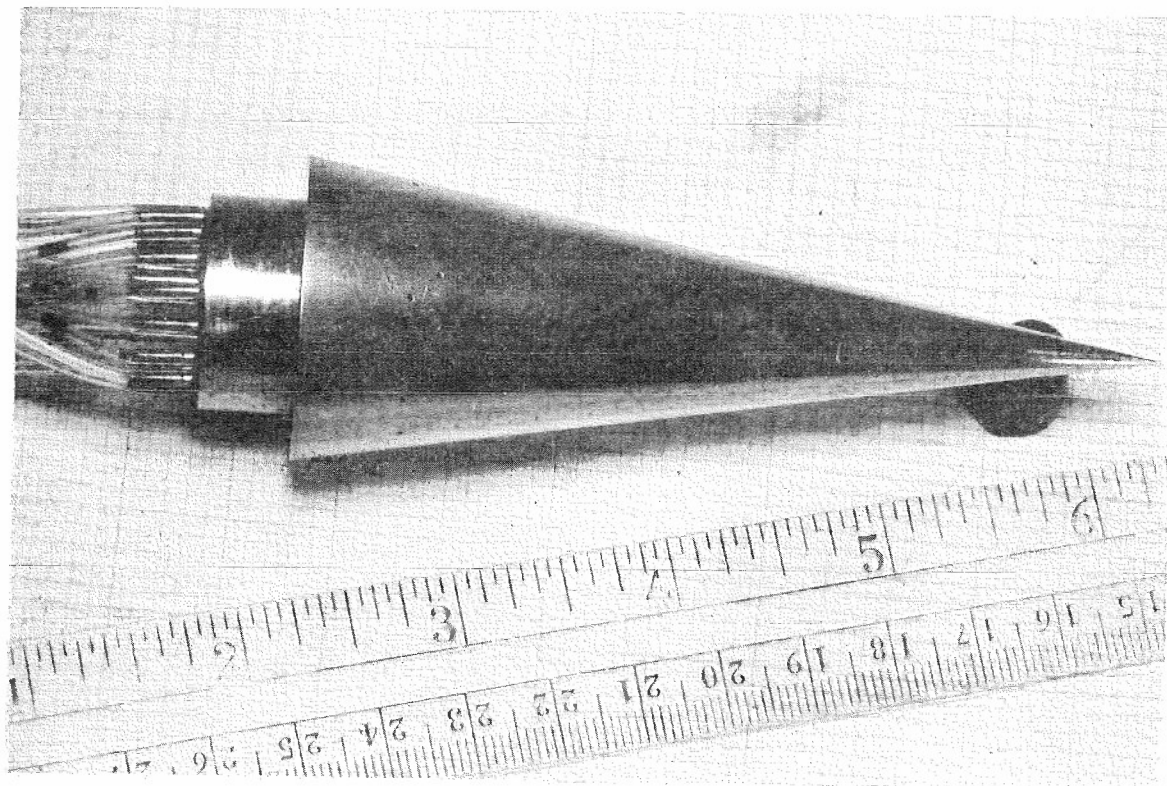


FIG. 5 15° CONE AND TUBES

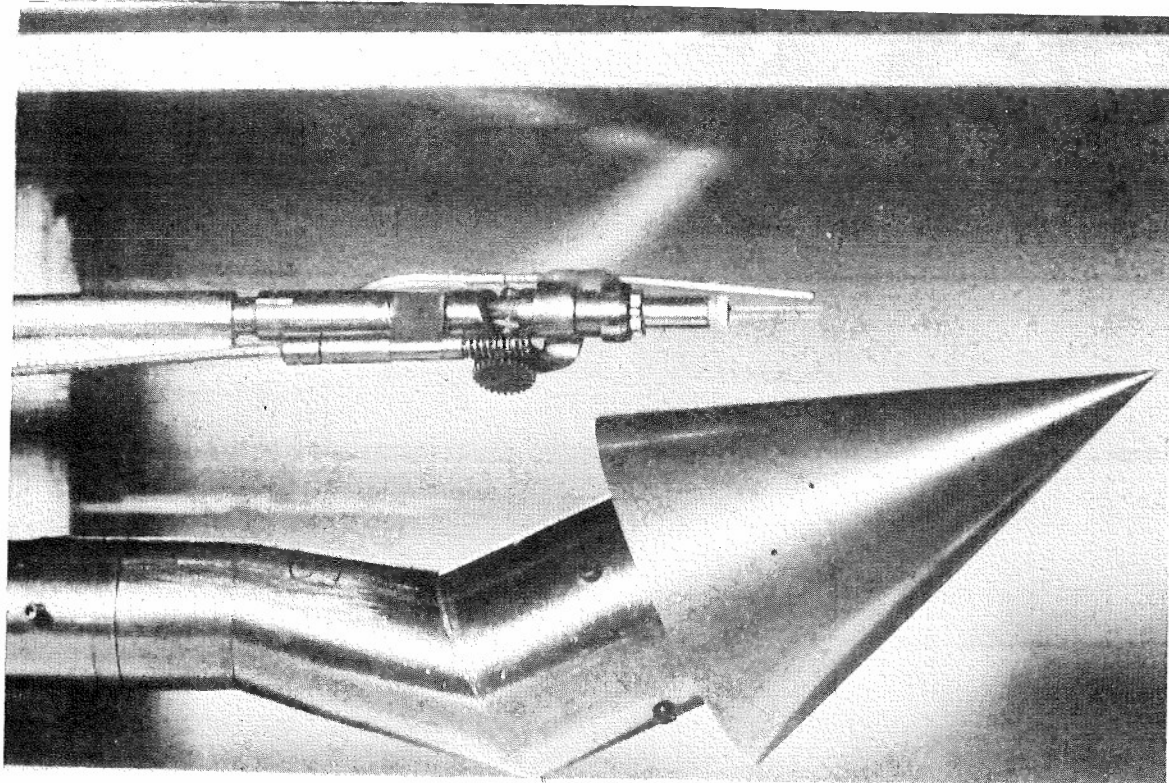


FIG. 6 20° CONE WITH ADAPTER AND PROBE

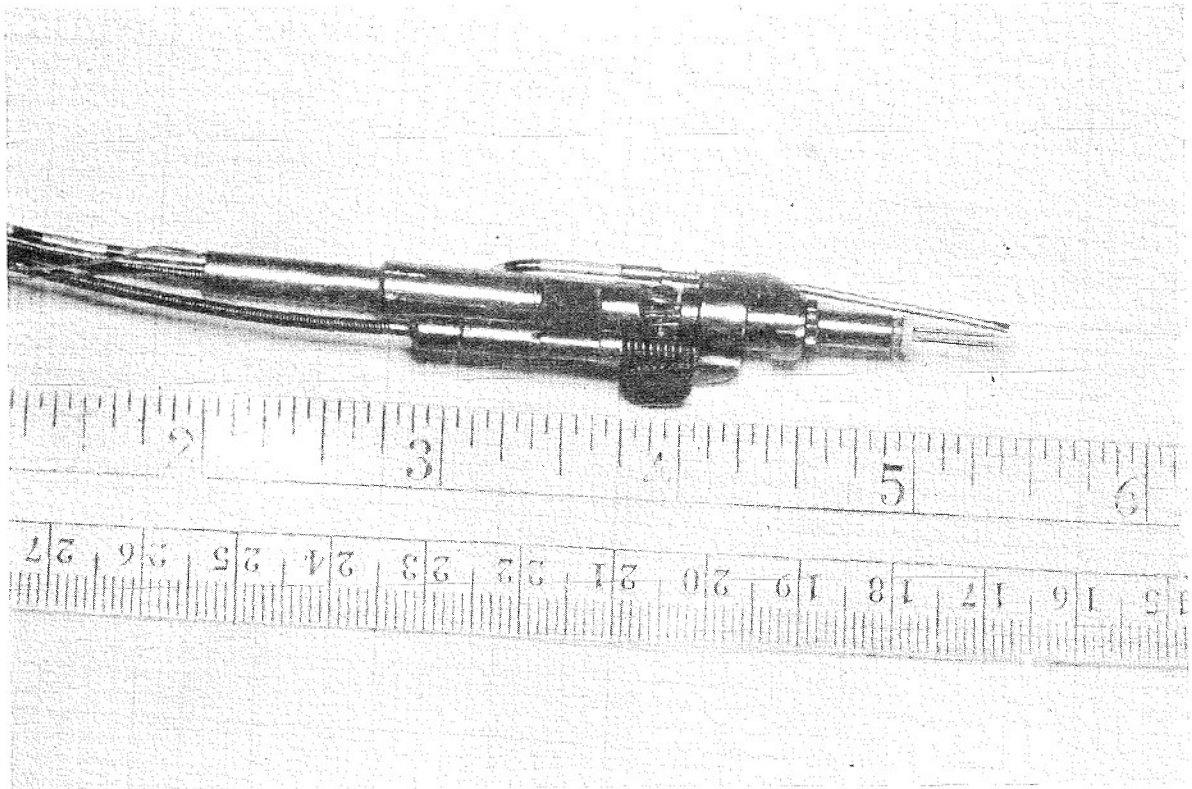


FIG. 7a HOT-WIRE- PITOT PROBE

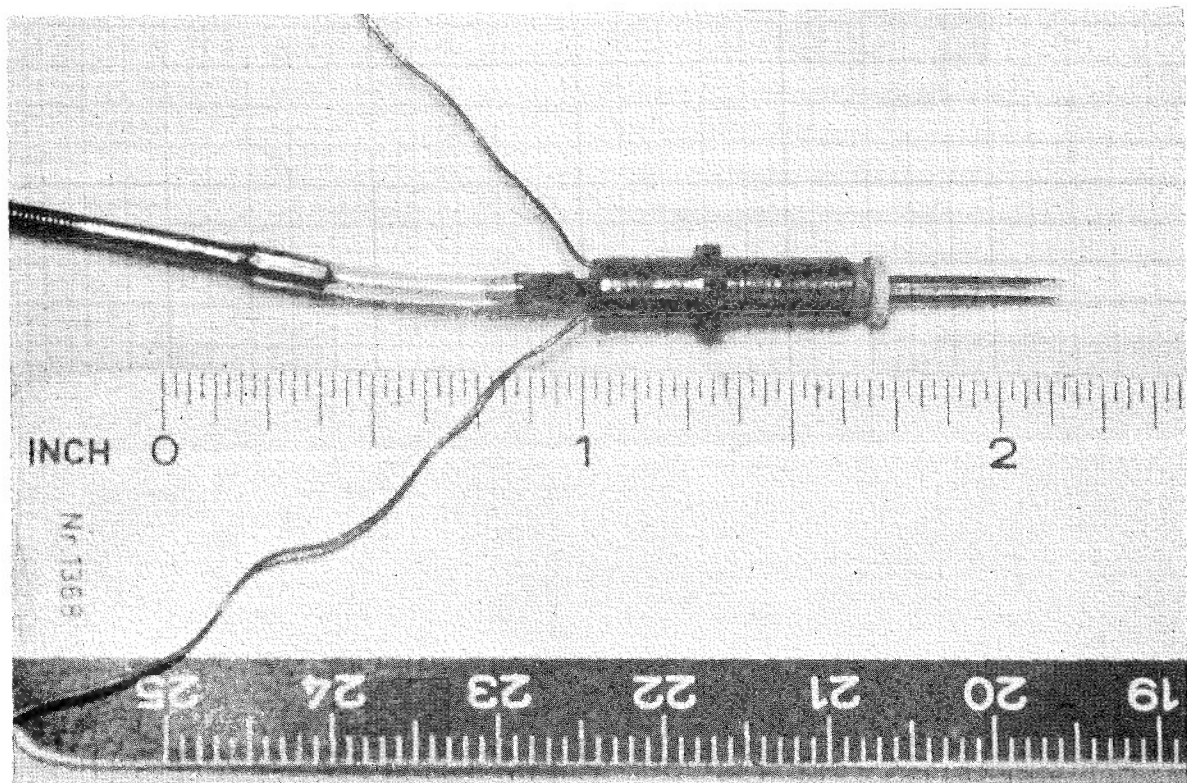
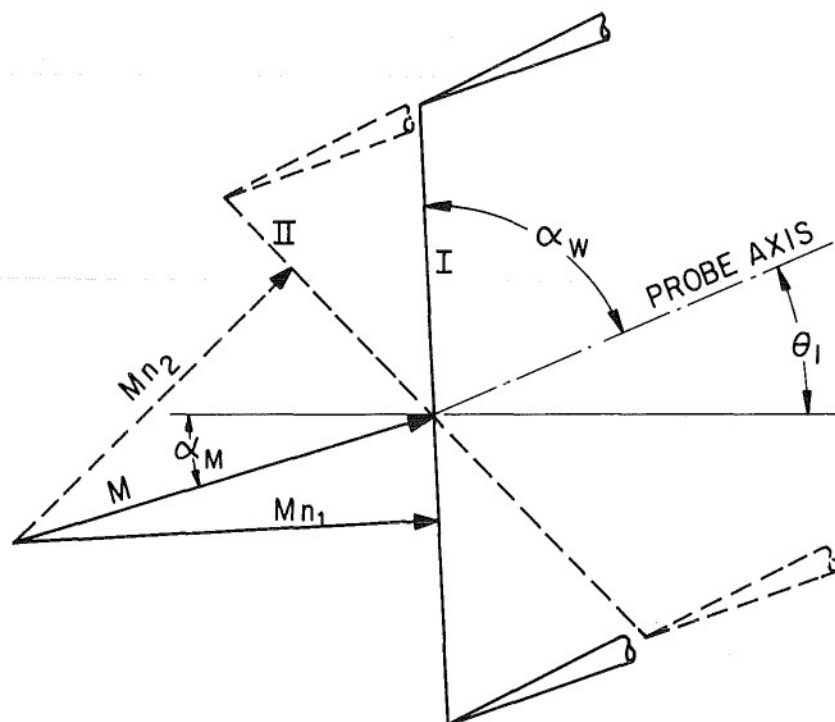


FIG. 7b THE ROTATING PART OF THE HOT-WIRE PROBE



NOTE: POSITION II IS ACHIEVED AFTER ROTATING THE HOT-WIRE PROBE 180° ABOUT ITS AXIS FROM POSITION I

FIG. 8 RELATIVE POSITION BETWEEN THE VELOCITY VECTOR AND THE HOT-WIRE IN THE PLANE $\phi = 180^\circ$



FIG. 9 COLOR SCHLIEREN OF 10° CONE AT $\alpha = 30^\circ$

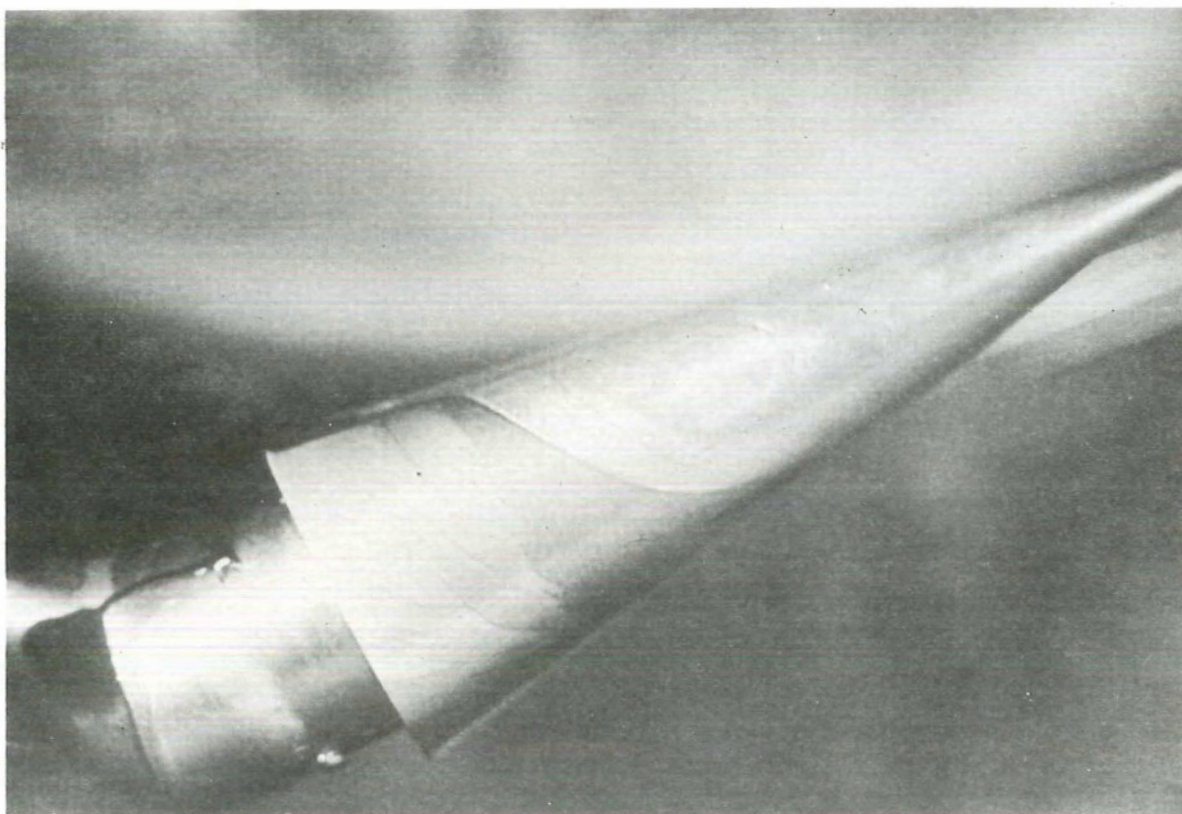


FIG. 10 OIL FLOW OVER 10° CONE AT $\alpha = 30^\circ$

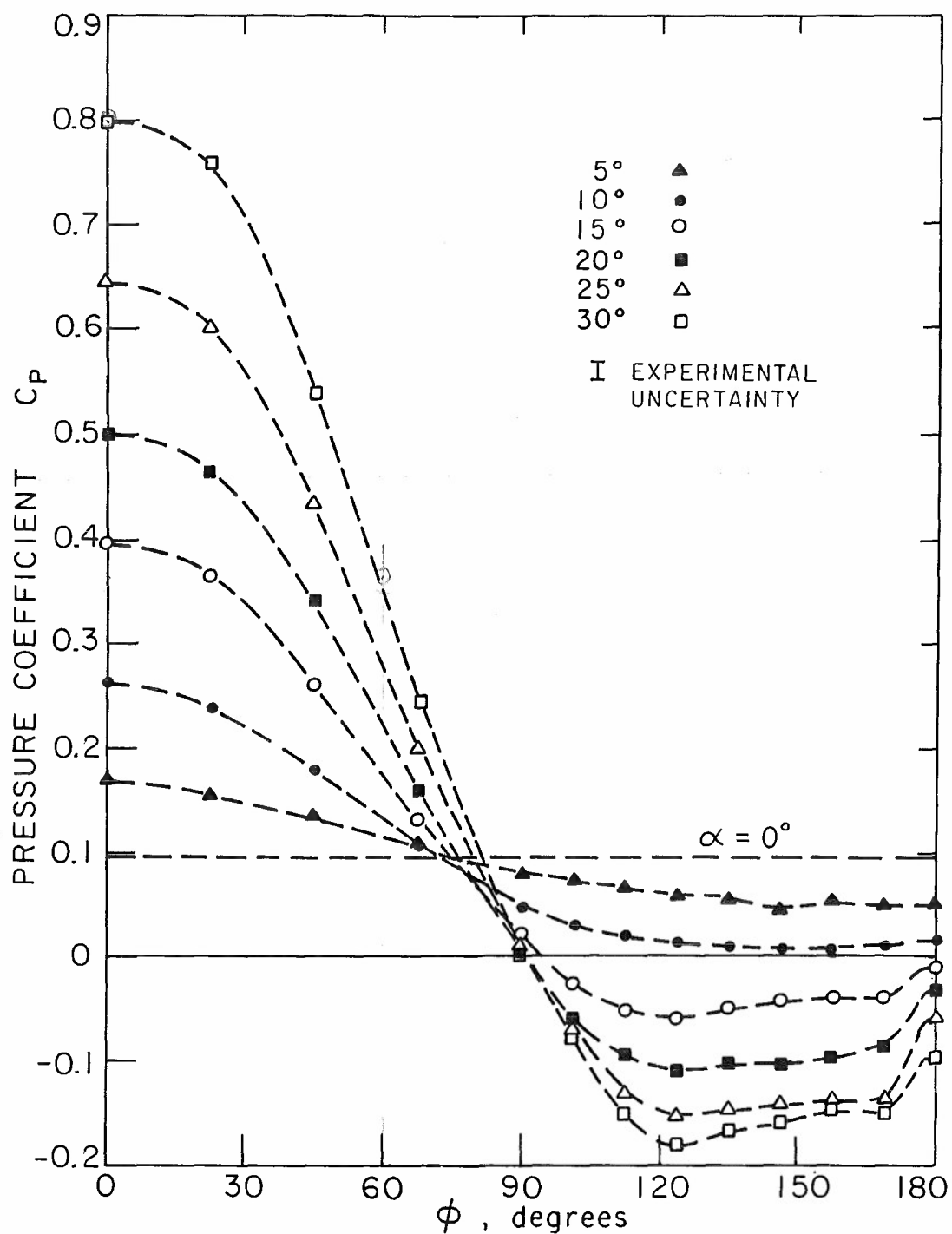


FIG. 11a CIRCUMFERENTIAL PRESSURE DISTRIBUTION FOR
A $\theta_c = 10^\circ$ CONE AT VARIOUS ANGLES OF ATTACK

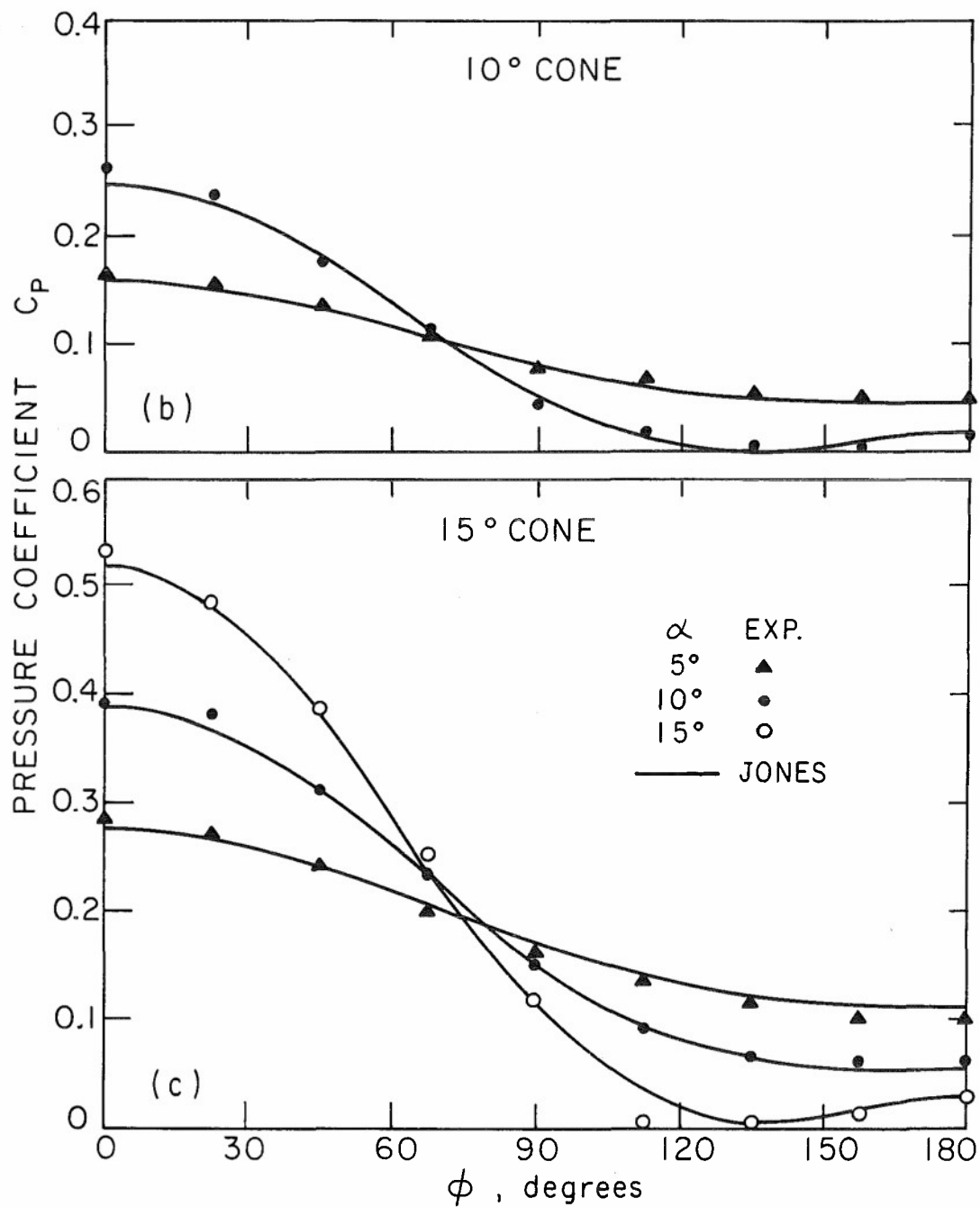


FIG. II b,c COMPARISON OF EXPERIMENTAL PRESSURE DISTRIBUTION WITH JONES' RESULTS

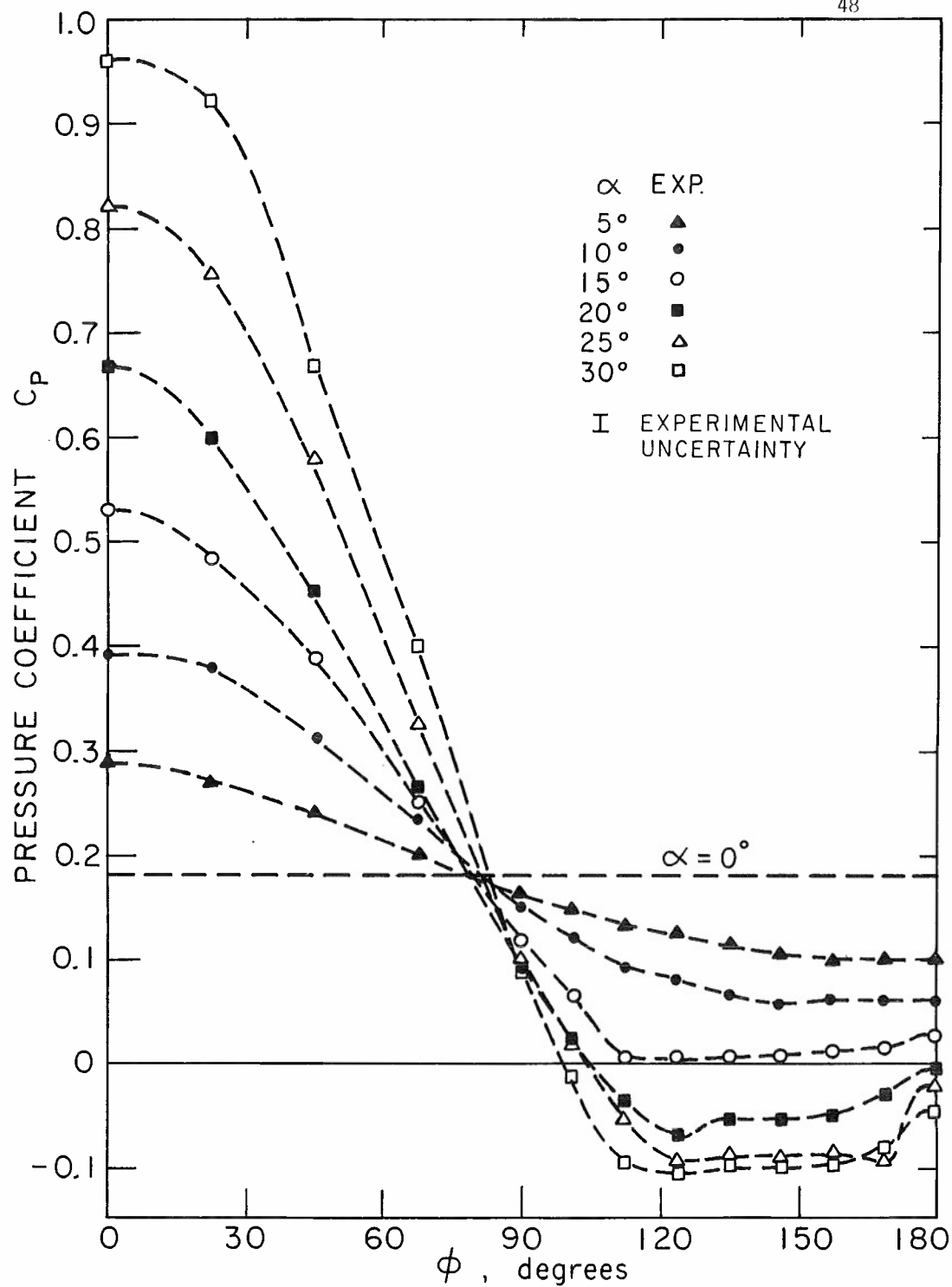


FIG. 11d CIRCUMFERENTIAL PRESSURE DISTRIBUTION FOR
A $\theta_c = 15^\circ$ CONE AT VARIOUS ANGLES OF ATTACK

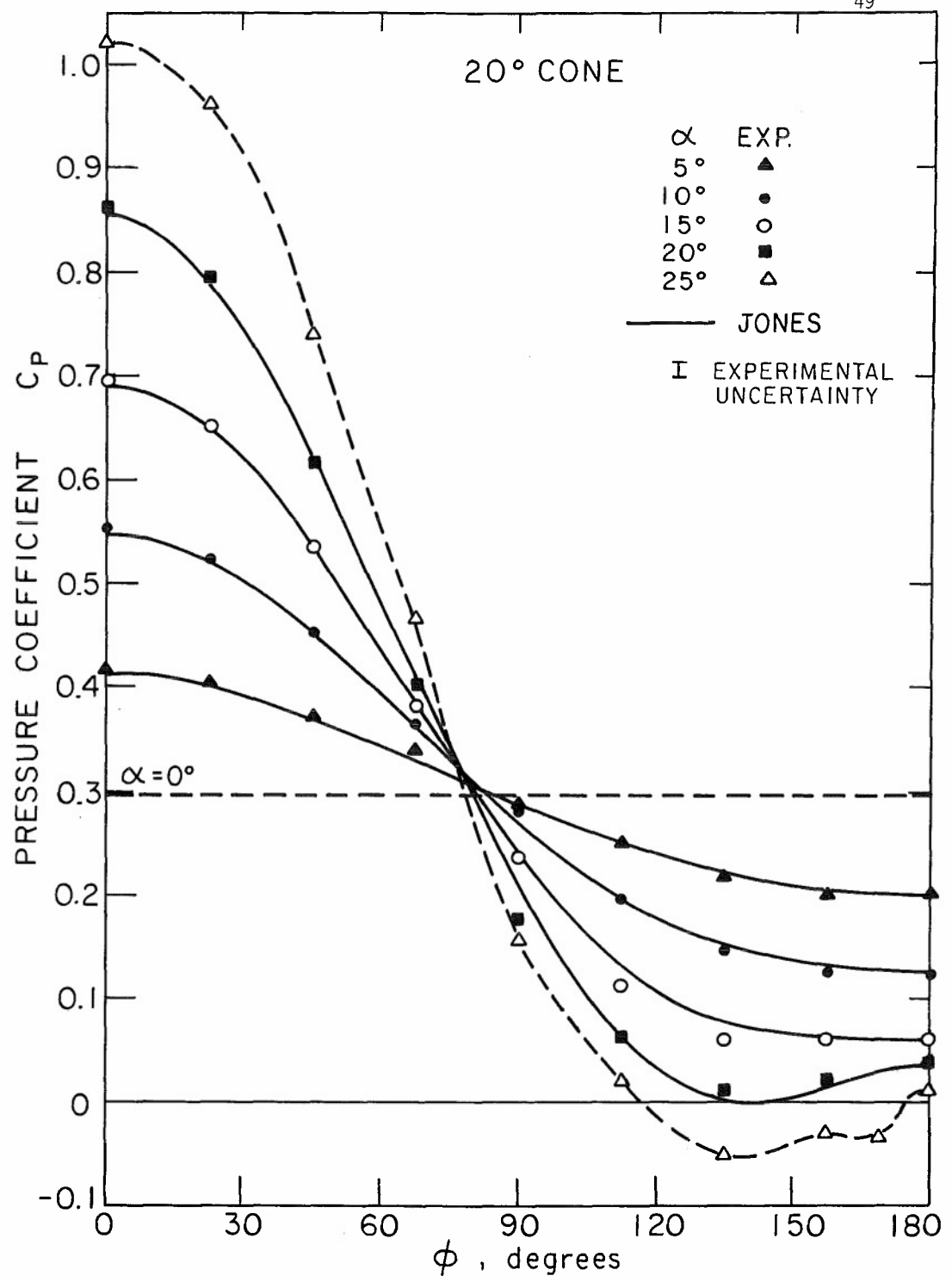


FIG. 11e COMPARISON OF EXPERIMENTAL PRESSURE DISTRIBUTION WITH JONES' RESULTS

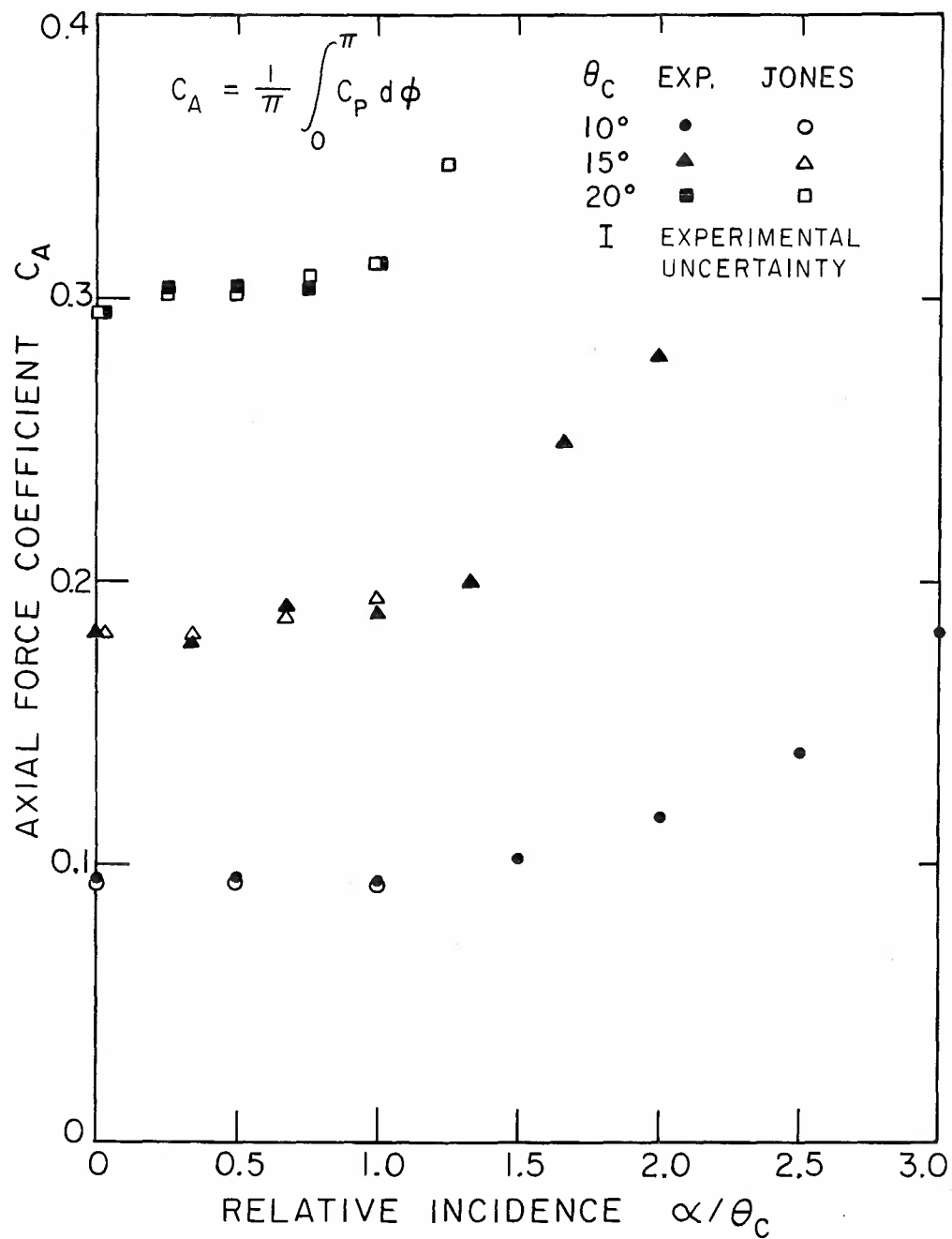


FIG. 12 AXIAL FORCE COEFFICIENT

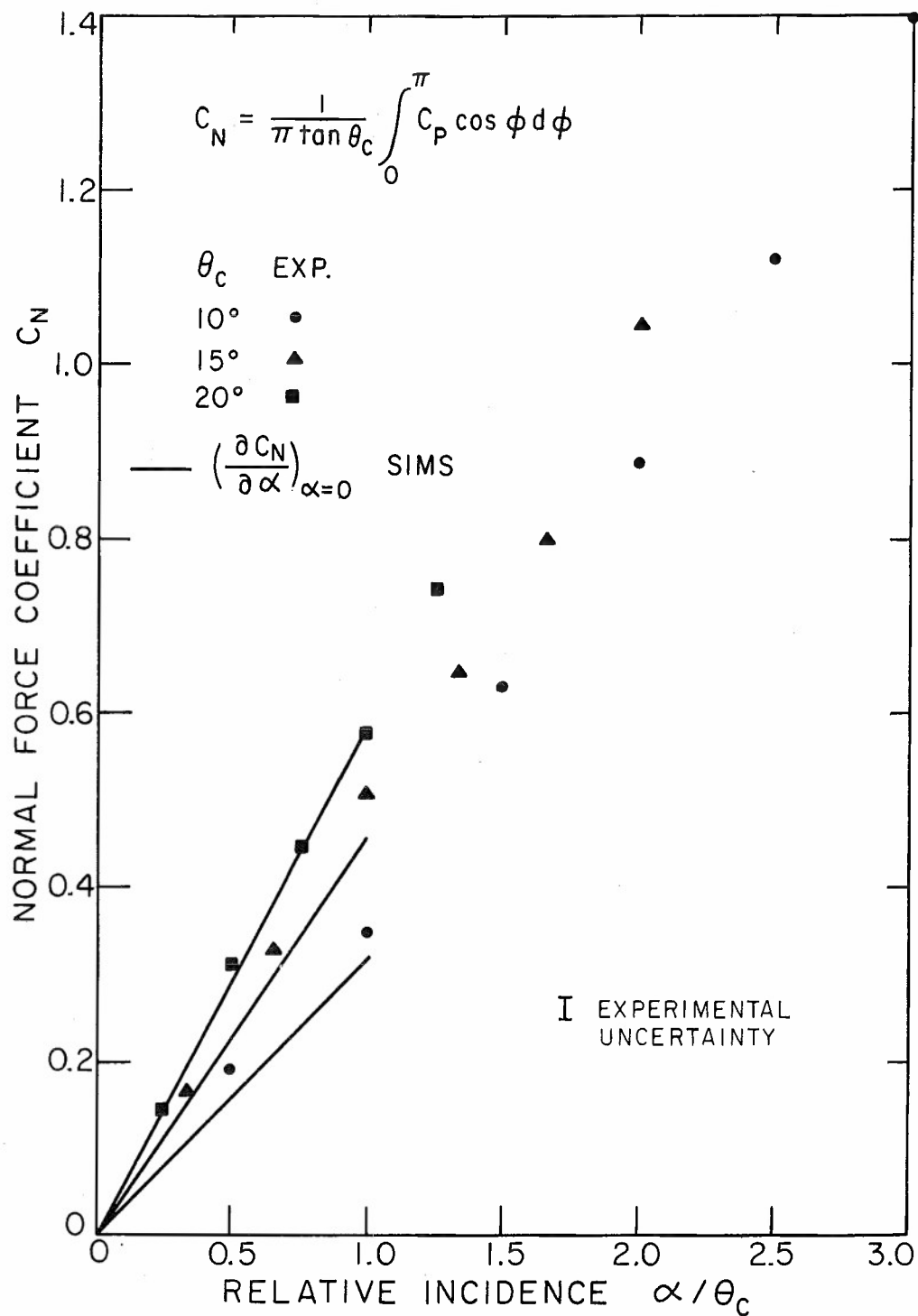


FIG. 13 NORMAL FORCE COEFFICIENT

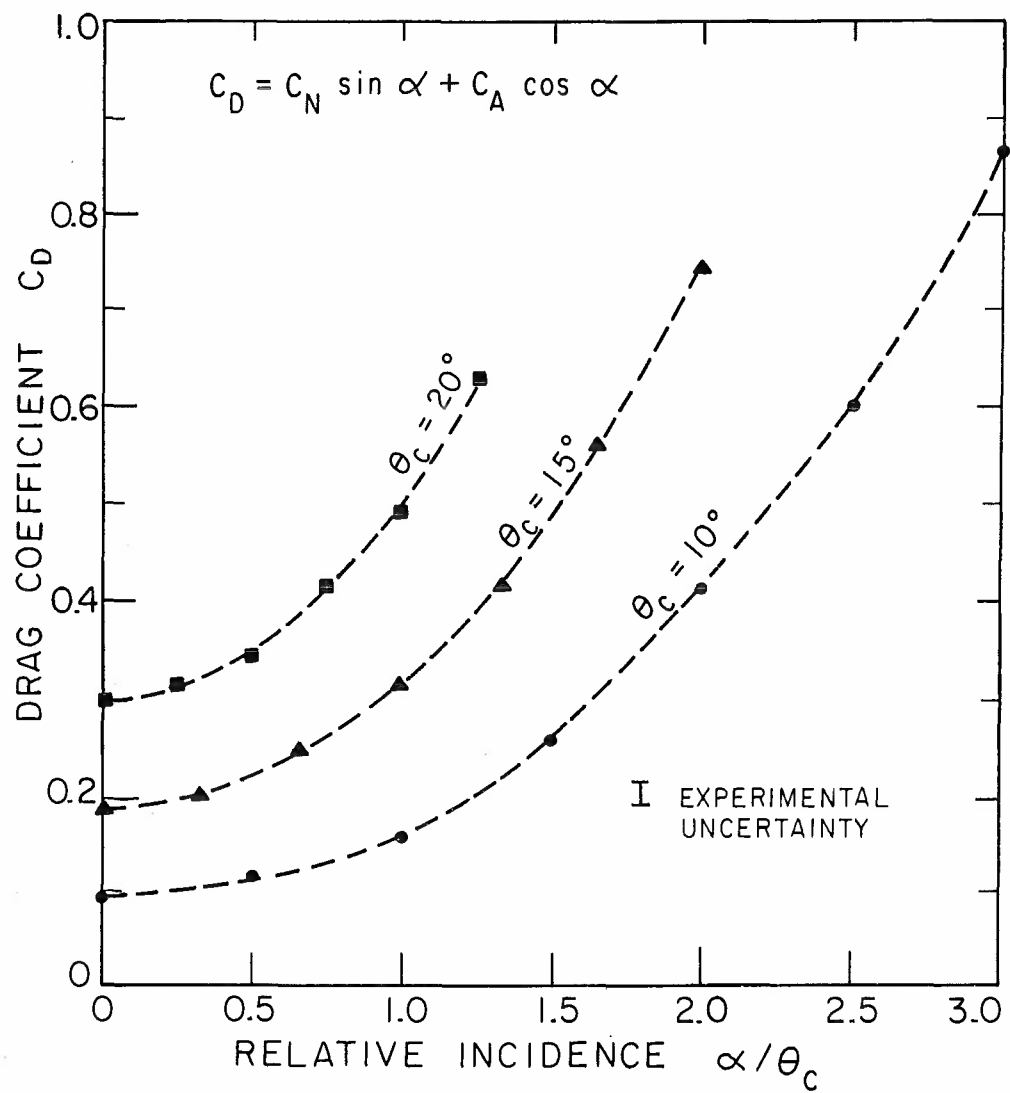


FIG. 14 DRAG COEFFICIENT

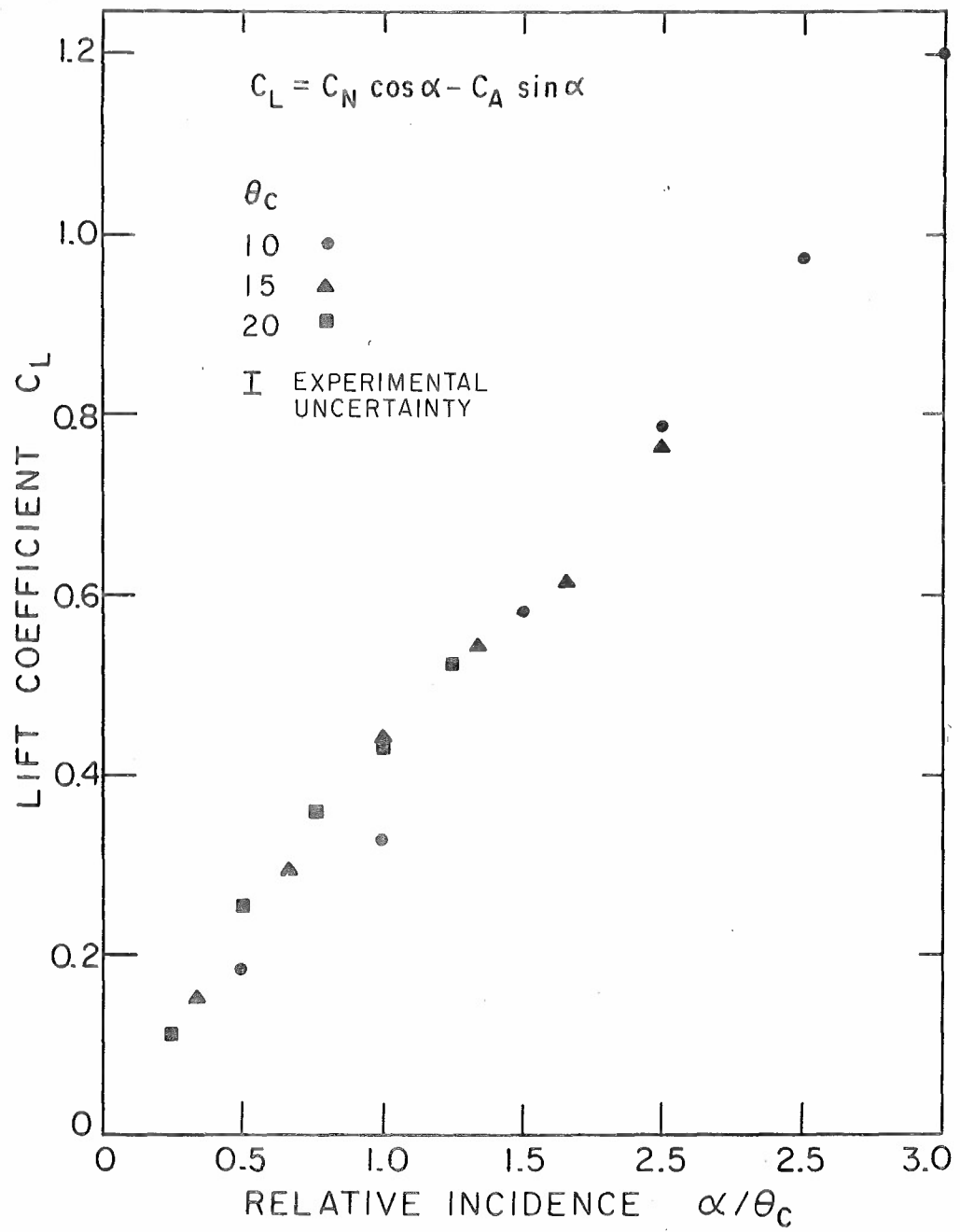


FIG. 15 LIFT COEFFICIENT

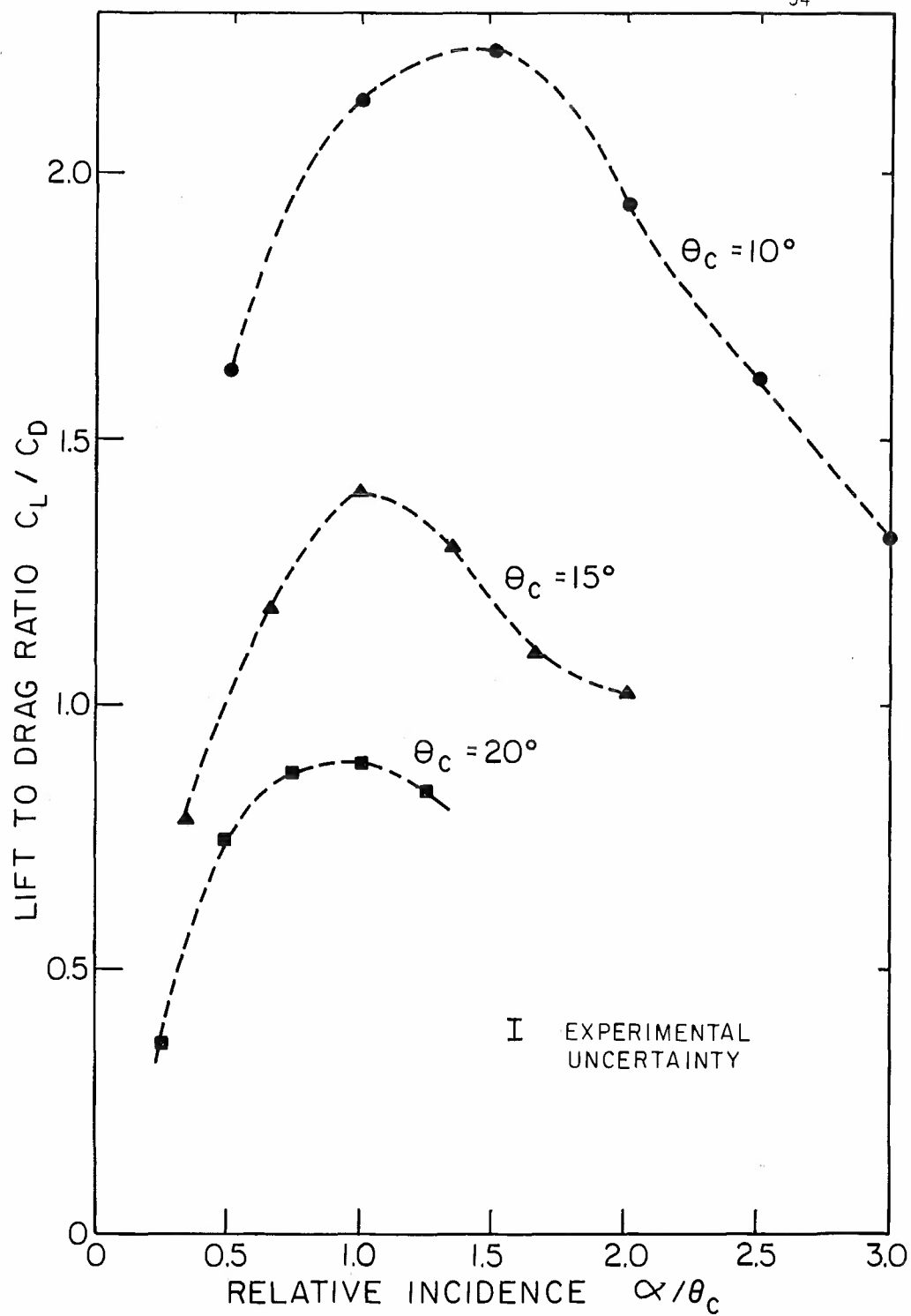


FIG. 16 LIFT TO DRAG RATIO

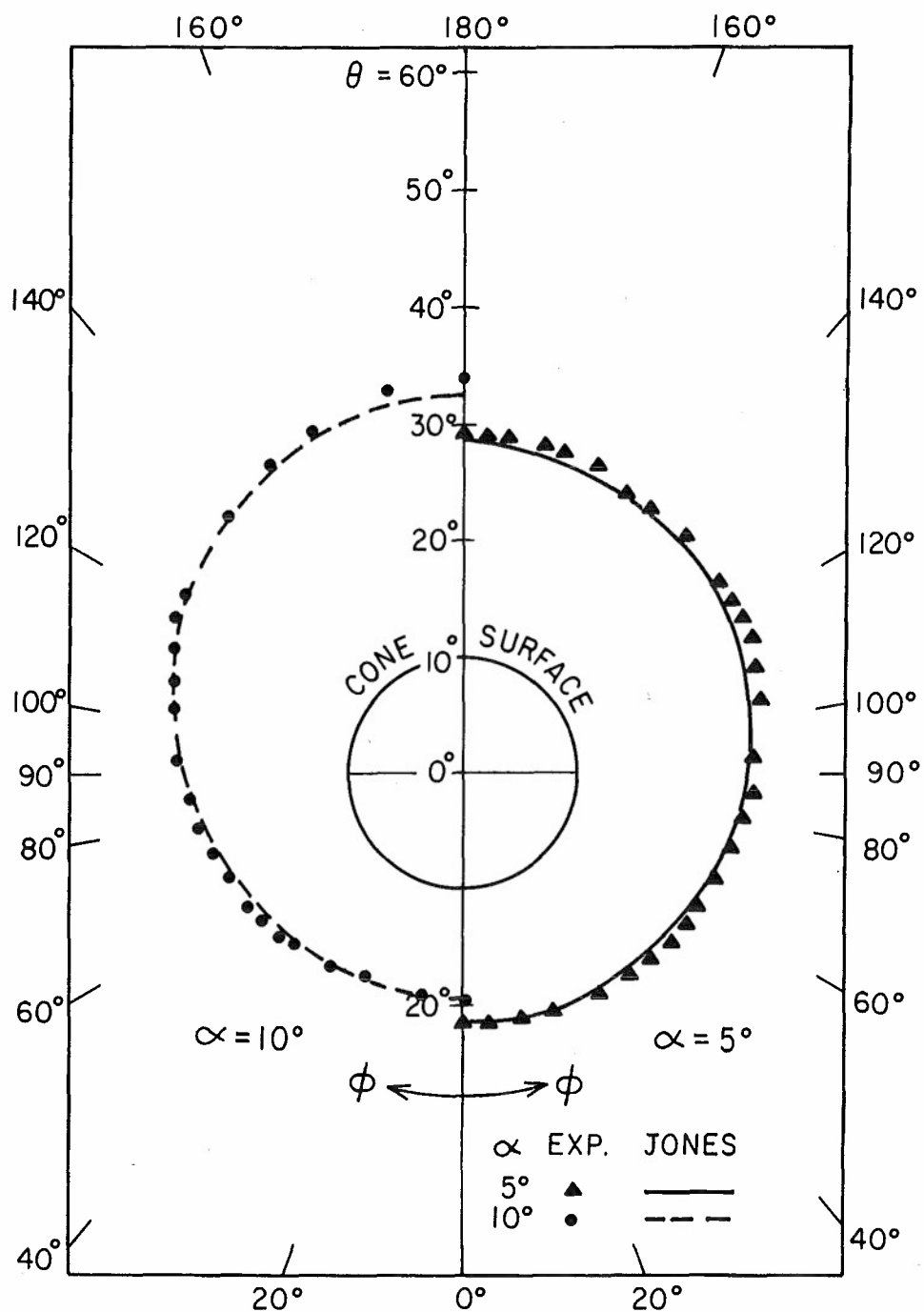


FIG. 17a OUTER SHOCK SHAPE FOR 10° CONE AT 5° AND 10° OF INCIDENCE

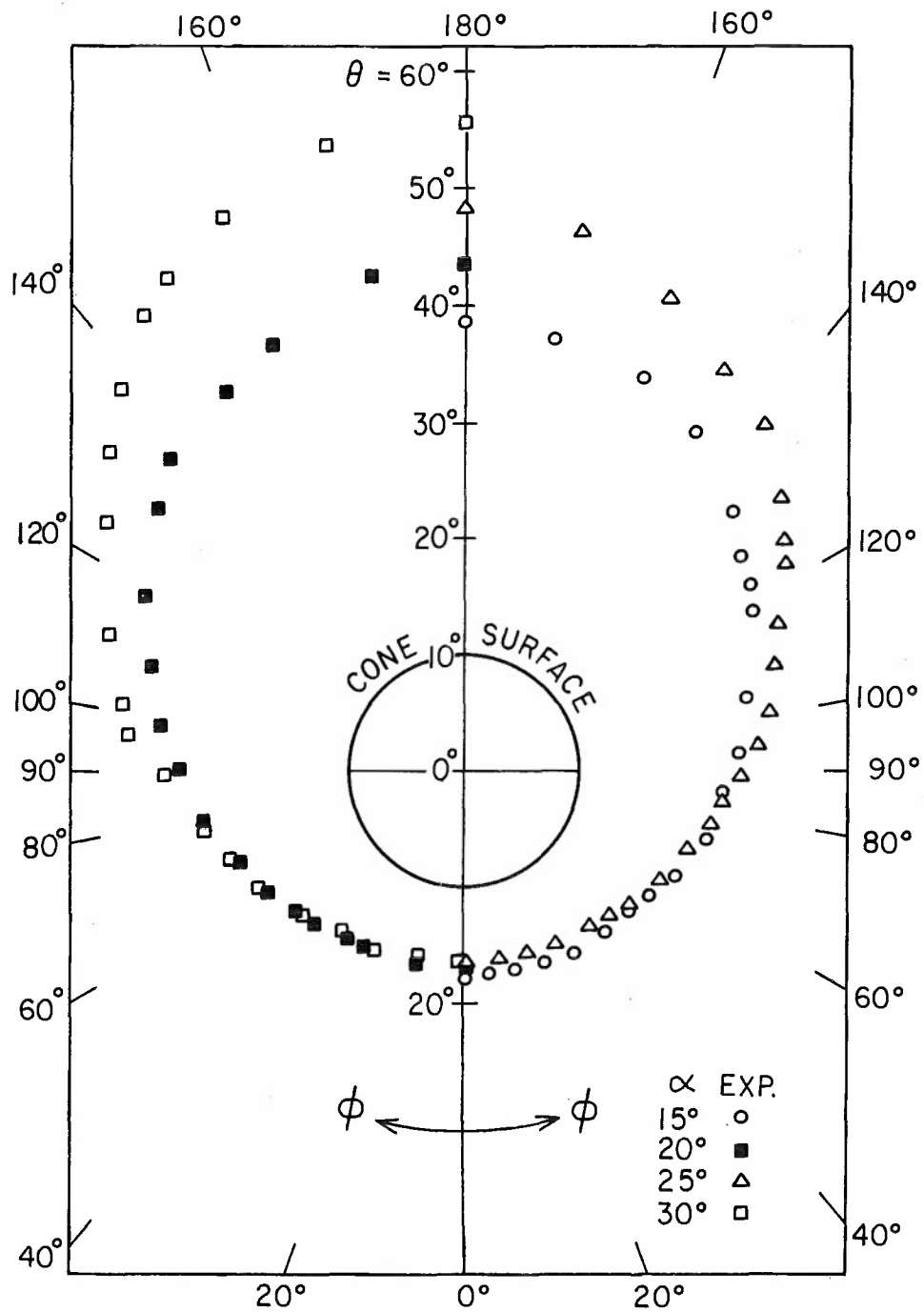


FIG. 17b OUTER SHOCK SHAPE FOR 10° CONE AT 15° , 20° , 25° , 30° OF INCIDENCE

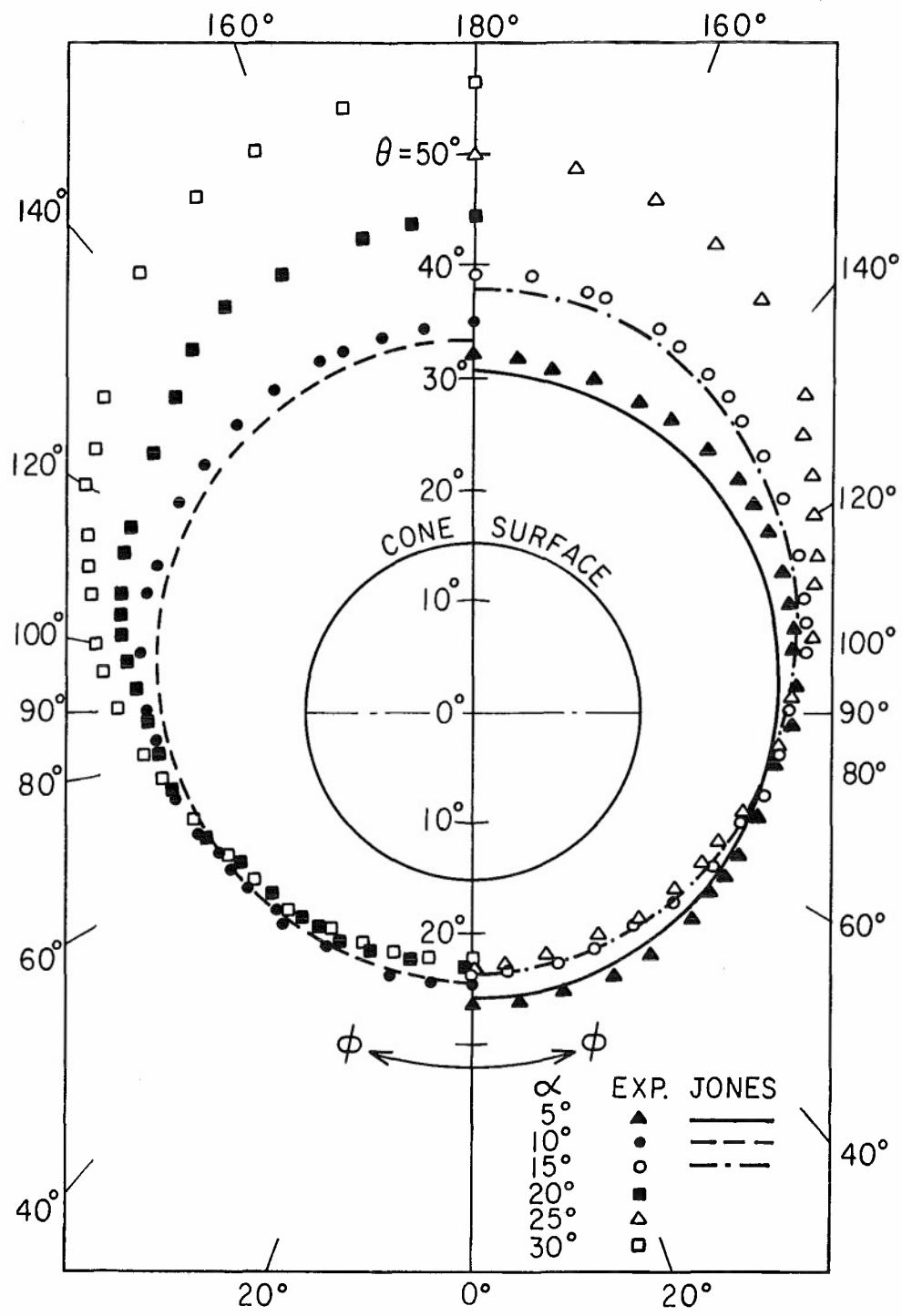


FIG. 17c OUTER SHOCK WAVE FOR 15° CONE

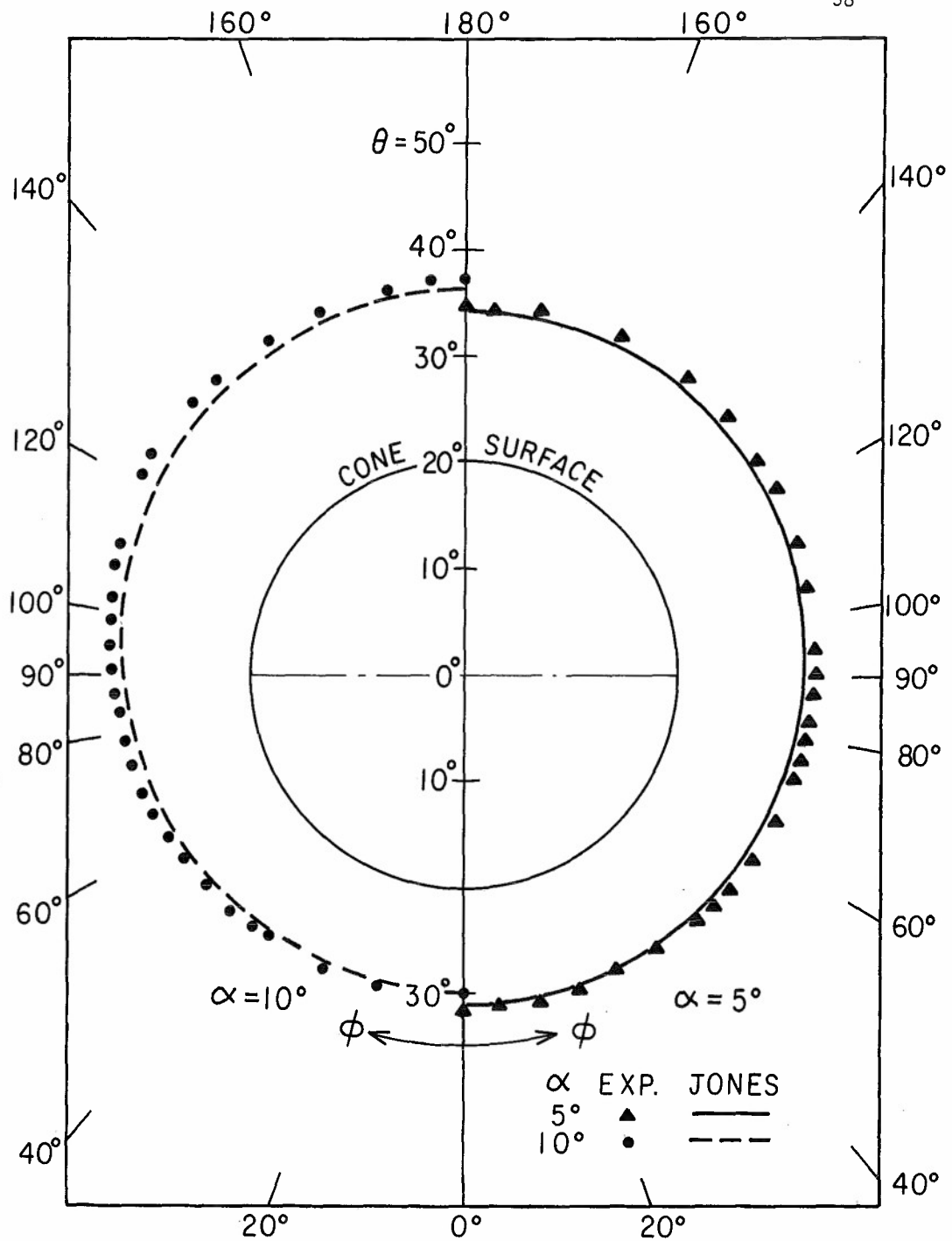


FIG. 17d OUTER SHOCK SHAPE FOR 20° CONE AT 5° AND 10° OF INCIDENCE

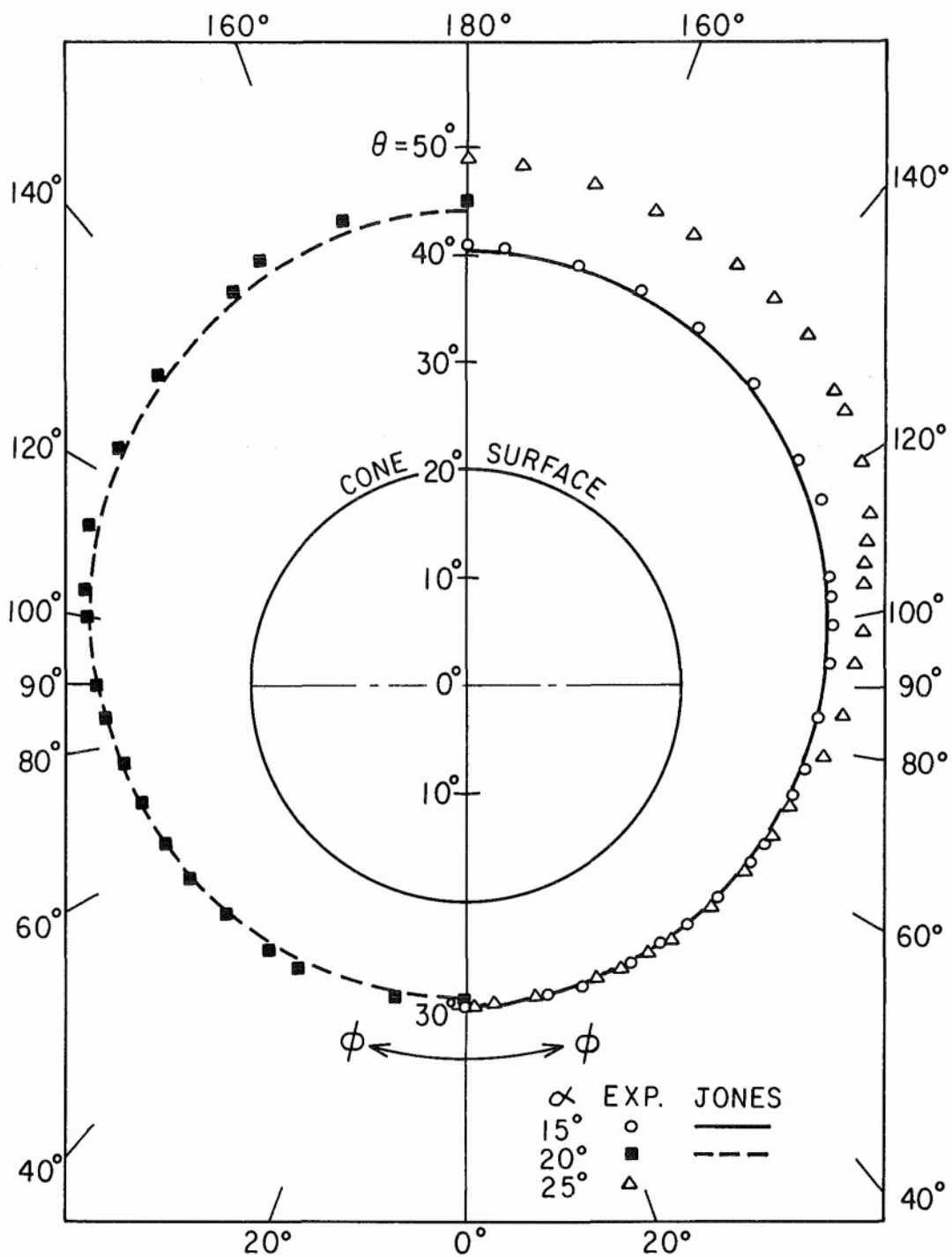


FIG. 17 e OUTER SHOCK SHAPE FOR 20° CONE AT 15°, 20° AND 25° OF INCIDENCE

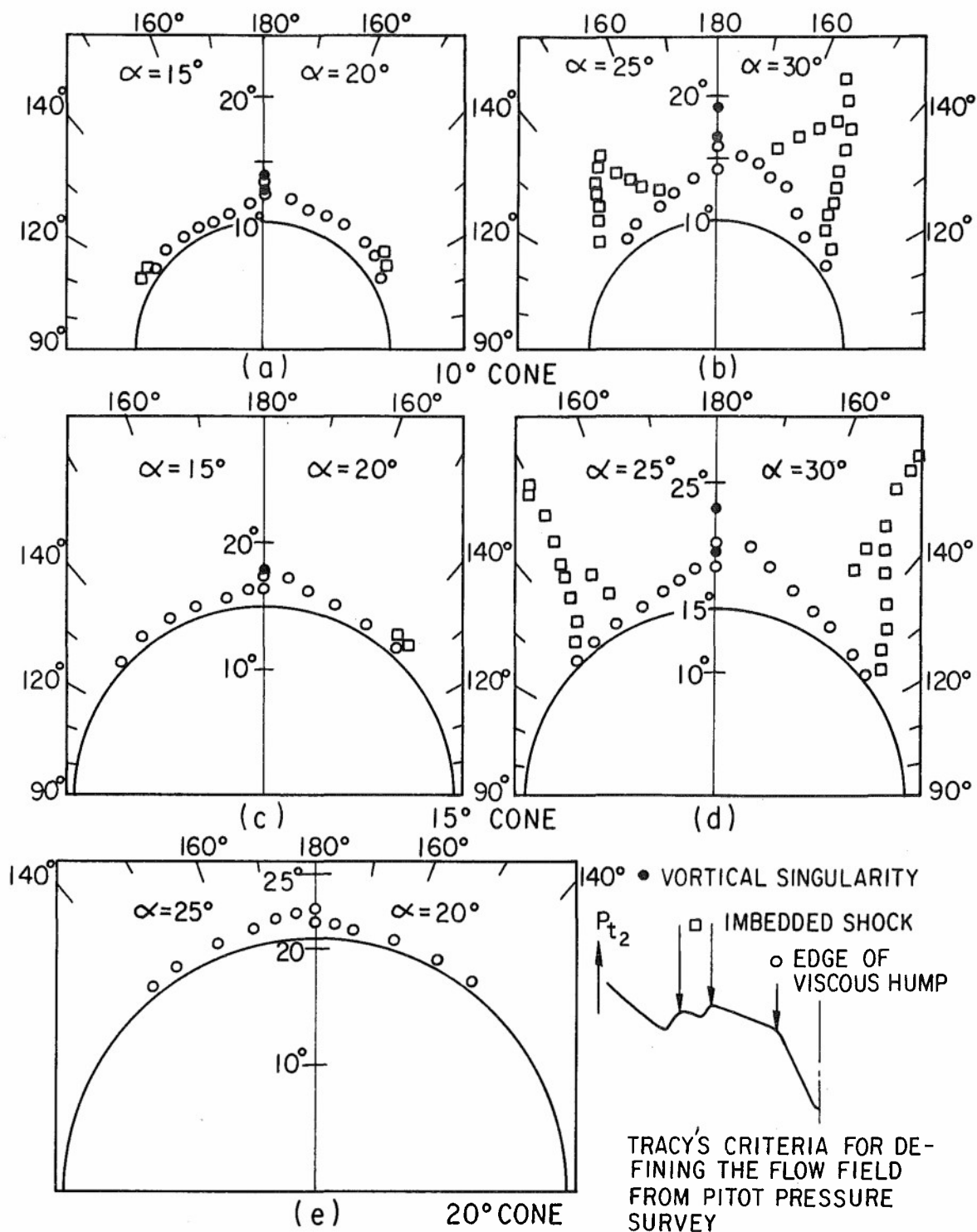
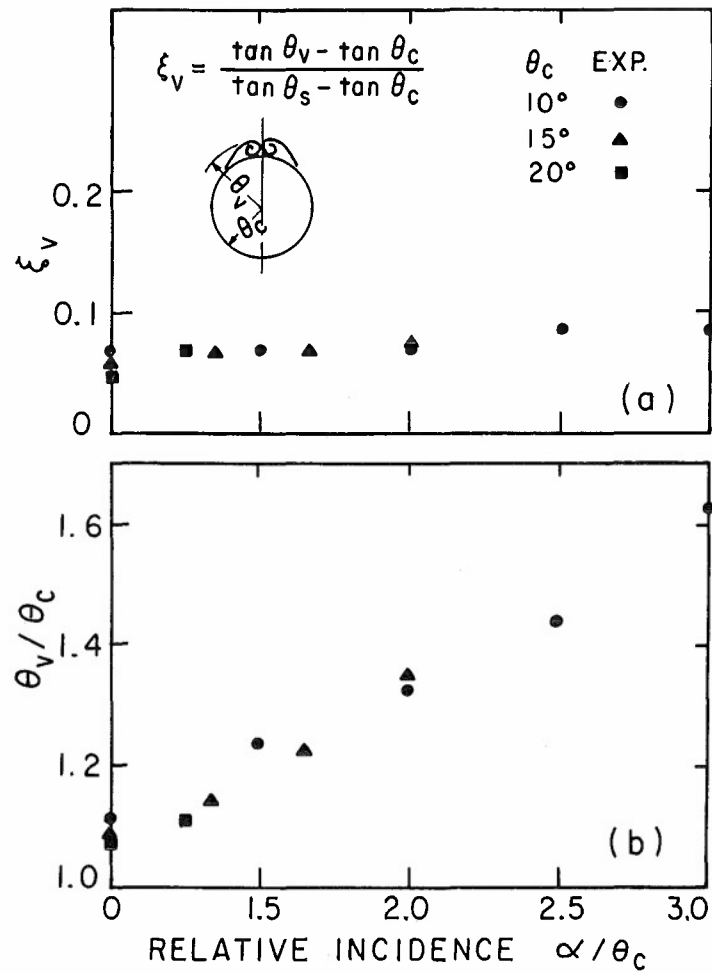


FIG. 18 IMBEDDED SHOCKS AND VISCOUS HUMP

FIG. 19 MAXIMUM VORTEX HEIGHT θ_c

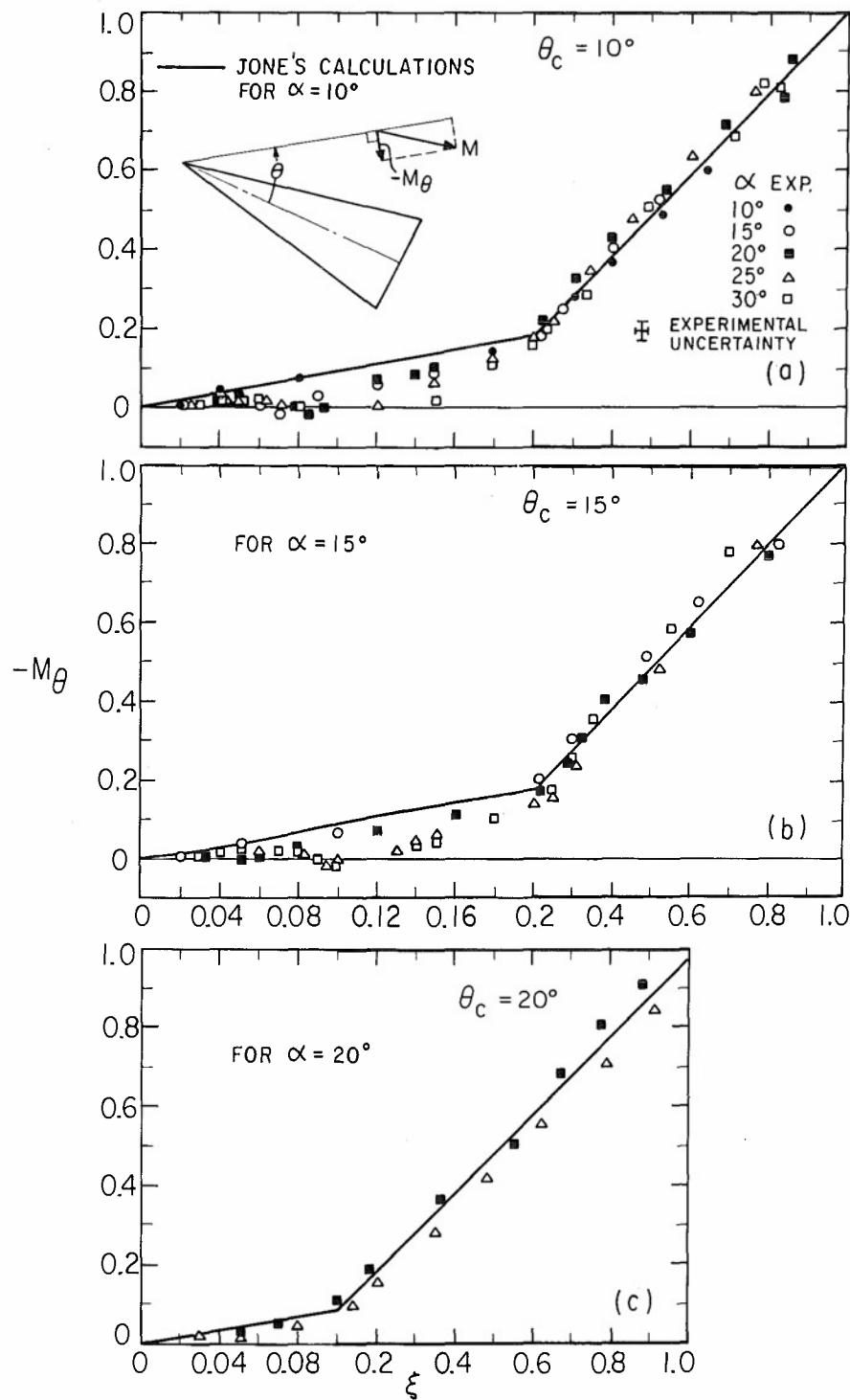


FIG. 20 MACH NUMBER COMPONENT IN THE θ DIRECTION IN THE $\phi = 180^\circ$ PLANE

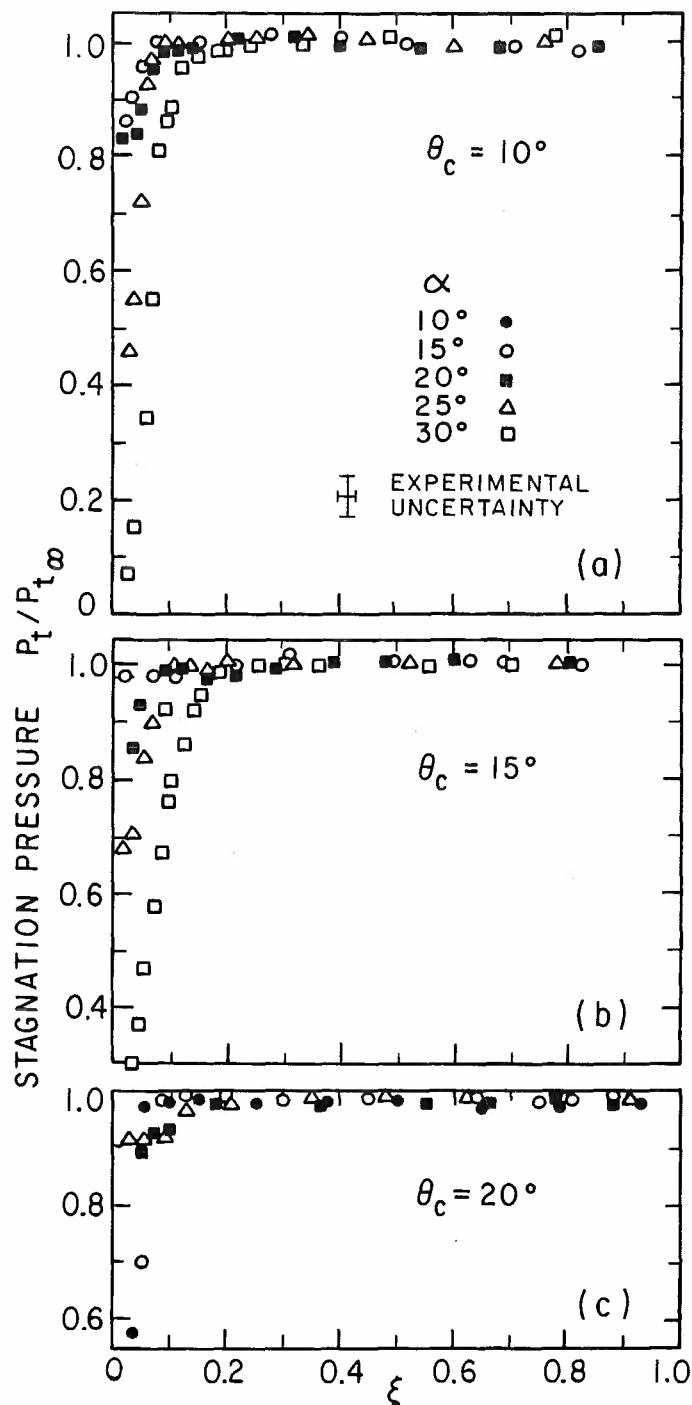


FIG. 21 STAGNATION PRESSURE DISTRIBUTION IN PLANE OF SYMMETRY $\phi = 180^\circ$

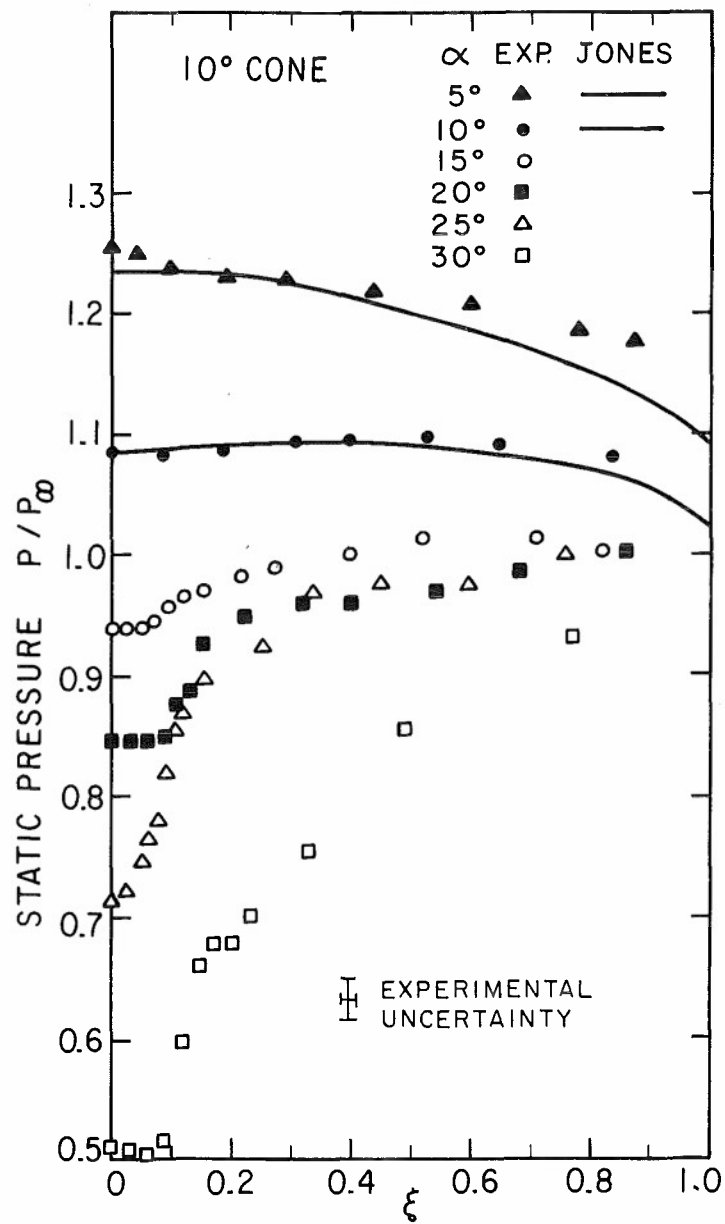


FIG. 22a STATIC PRESSURE DISTRIBUTION IN
PLANE OF SYMMETRY $\phi = 180^\circ$

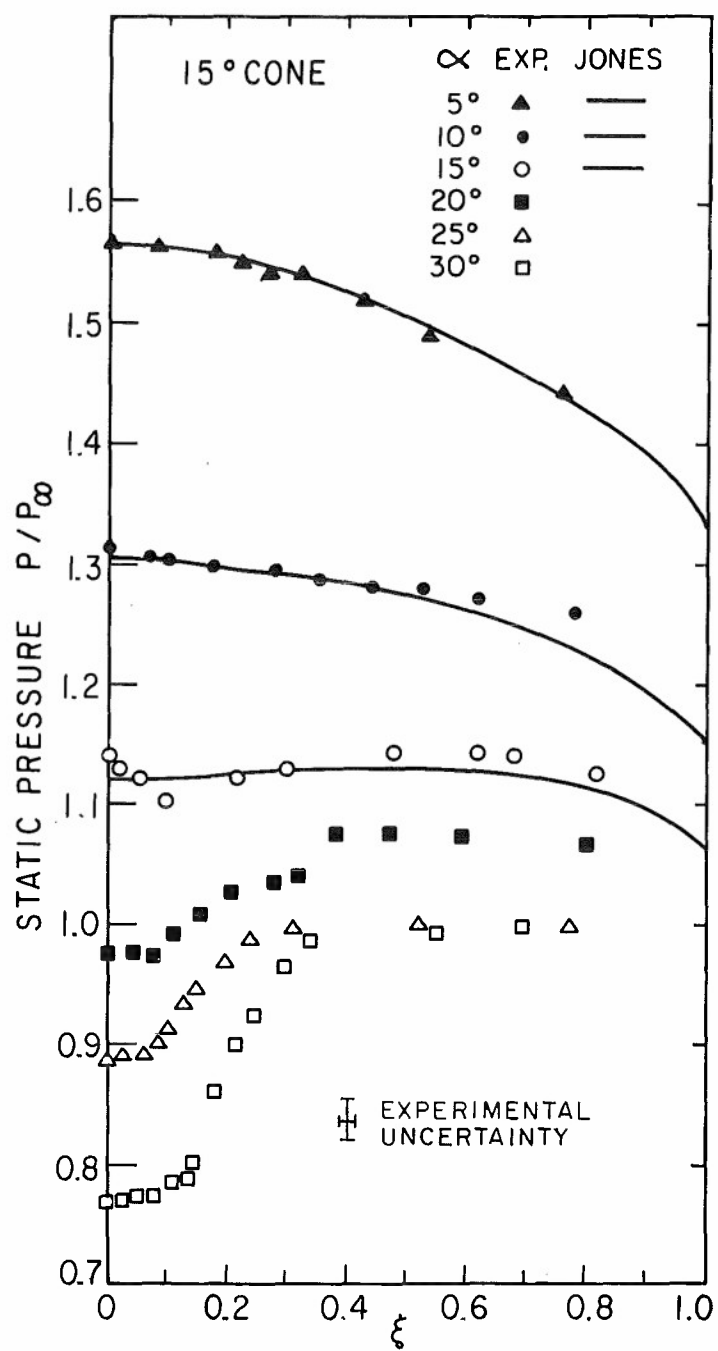


FIG. 22b STATIC PRESSURE DISTRIBUTION IN PLANE OF SYMMETRY $\phi=180^\circ$

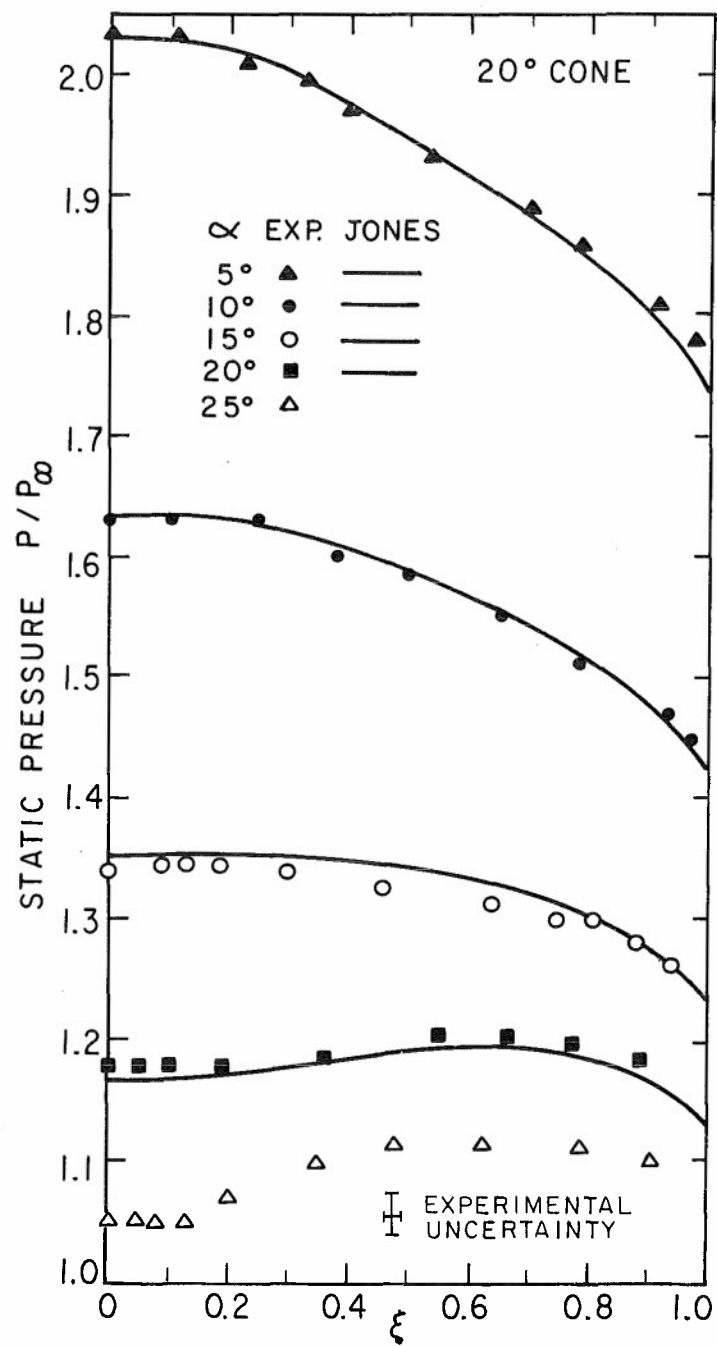


FIG. 22c STATIC PRESSURE DISTRIBUTION IN PLANE OF SYMMETRY $\phi = 180^\circ$

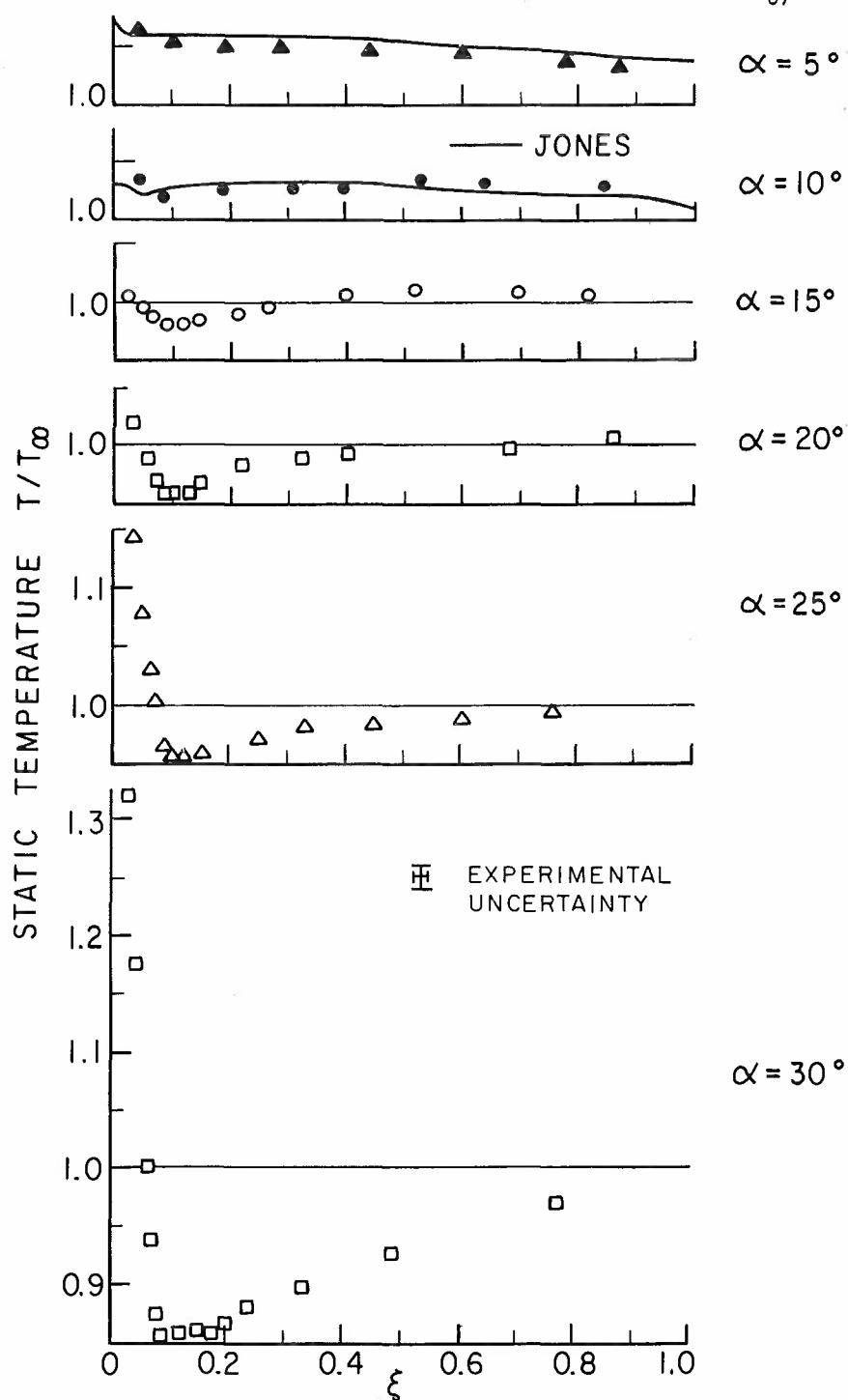


FIG. 23a STATIC TEMPERATURE DISTRIBUTION IN PLANE OF SYMMETRY $\phi = 180^\circ$ FOR 10° CONE

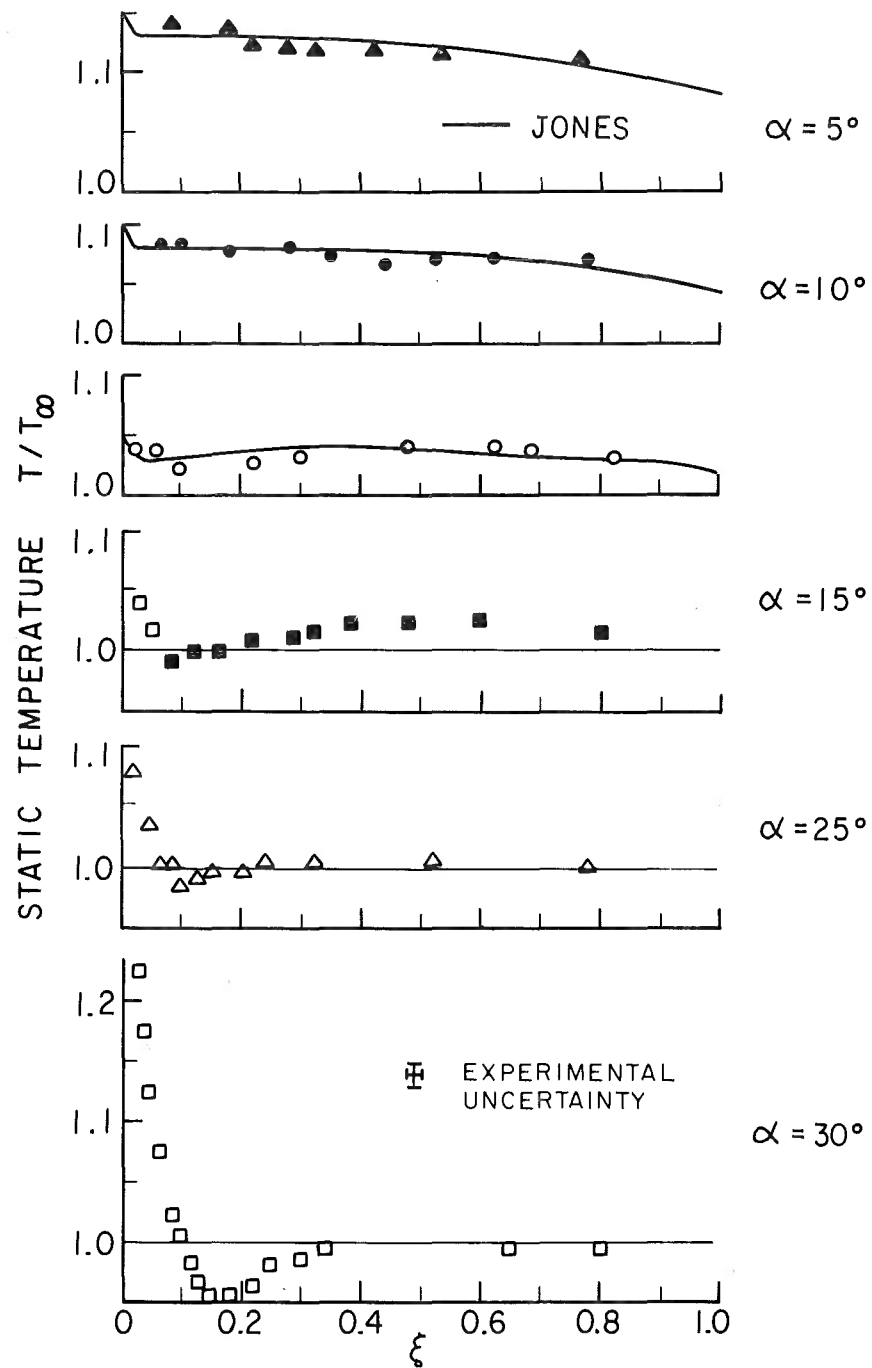


FIG. 23b STATIC TEMPERATURE DISTRIBUTION IN PLANE OF SYMMETRY $\phi = 180^\circ$ FOR 15° CONE

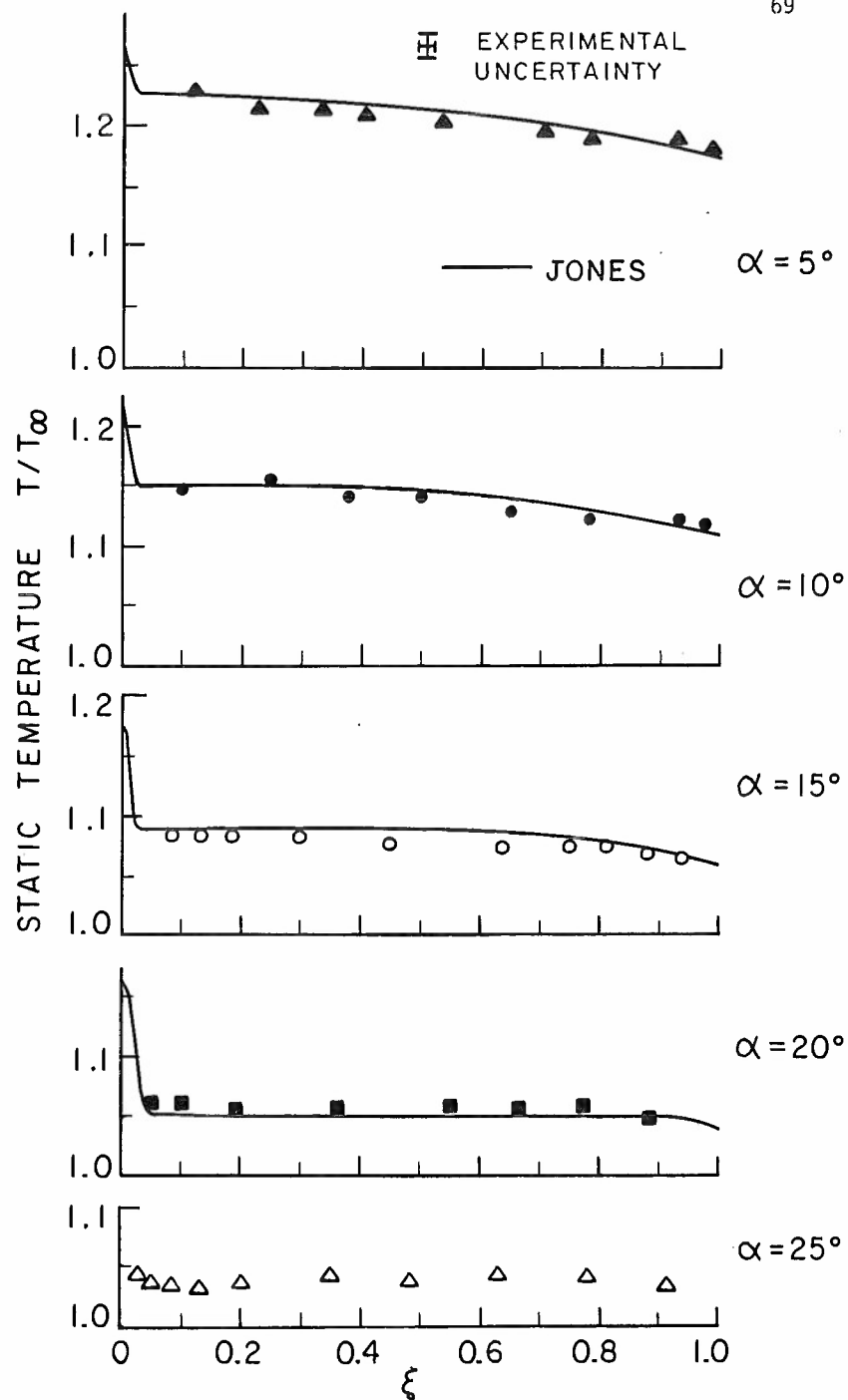


FIG. 23c STATIC TEMPERATURE DISTRIBUTION IN PLANE OF SYMMETRY $\phi = 180^\circ$ FOR 20° CONE

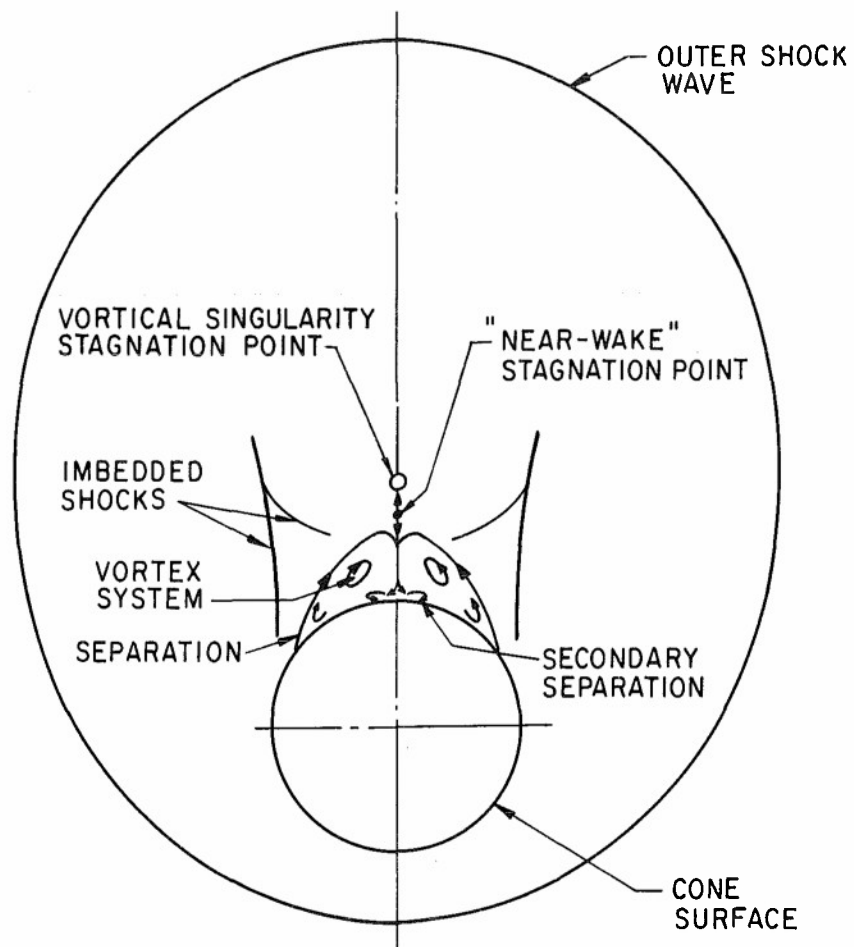


FIG. 24 FLOW FIELD AROUND A CONE AT A LARGE ANGLE OF ATTACK

APPENDIX

1. END LOSS CORRECTION FACTORS

The Nusselt number end loss correction factor is given by:
(Kovaszny, 1954)

$$C_{Nu} = \frac{\bar{a}_w}{a_w^*} \frac{1 + a_w^*}{1 + \bar{a}_w}$$

where \bar{a}_w/a_w^* is given in Fig. A-1 as a function of S , and
 $\bar{a}_w = (R_w - R_e)/R_e$.

The recovery temperature correction factor is given by:
(Dewey, 1961)

$$C_R = [1 - \omega \left(\frac{\eta_n}{\eta_m} \right)] (1 - \omega)^{-1}$$

where $\omega/(1 - \omega)$ is given in Fig. A-1 as a function of S .

The recovery factor used for the recovery temperature of the support needles was 0.851 (Schlichting, p. 319). The temperature of the needles was computed from

$$T_n = T_t \cdot \frac{1 + 0.17 M^2}{1 + 0.2 M^2}$$

2. HEAT LOSS AND RECOVERY TEMPERATURE

The empirical formulas as were derived by Dewey and as used in reducing the hot wire data were as follows:

$$Nu_0(Re_0, M) = Nu_0(Re_0, \infty) \Phi(Re_0, M)$$

where

$$Nu_o(Re_o, \infty) = Re_o^n [0.14 + N_1 + N_2] ,$$

with:

$$n = 1 - \frac{Re_o^{0.6713}}{5.142 + 2 Re_o^{0.6713}}$$

$$N_1 = \frac{0.2302 Re_o^{0.7114}}{15.44 + Re_o^{0.7114}}$$

$$N_2 = \left(\frac{0.01569}{0.3077 + Re_o^{0.7378}} \right) \left(\frac{5}{15 + Re_o^3} \right)$$

and

$$\Phi(Re_o, M) = 1 + \phi_1 \times \phi_2 \times \phi_3$$

with

$$\phi_1 = \frac{0.6039}{M} + 0.5701 \left[\left(\frac{M^{1.222}}{1 + M^{1.222}} \right)^{1.569} - 1 \right]$$

$$\phi_2 = 1.834 - 1.634 \left(\frac{Re_o^{1.109}}{2.765 + Re_o^{1.109}} \right)$$

$$\phi_3 = 1 + \left(0.300 - \frac{0.065}{M^{1.67}} \right) \left(\frac{Re_o}{4 + Re_o} \right)$$

The relations giving \bar{n}_* , η_f and η_{co} are the following:

$$\bar{n}_* = \frac{Kn_\infty^{1.193}}{0.4930 + Kn_\infty^{1.193}}$$

$$\eta_{co} = 1 - 0.05 \left(\frac{M^{3.5}}{1.175 + M^{3.5}} \right)$$

and

$$\eta_f - \eta_{co} = 0.2167 \left(\frac{M^{2.8}}{0.8521 + M^{2.8}} \right)$$

As is noted in Section 3.4.2.1, Re_o can be expressed in terms of M , T_t , P_{t_2} ,

$$Re_o = \frac{\rho U d}{\mu_t} = \sqrt{\frac{\gamma}{R}} \frac{P_t M}{\mu_t \sqrt{T_t}} (1 + \frac{\gamma-1}{2} M^2)^{-3}$$

using the relation for P_{t_2}/P_t from NACA Report No. 1135 and $\gamma = 1.4$, one gets,

$$Re_o = \sqrt{\frac{1.4}{R}} \frac{P_{t_2} M d}{\mu_t T_t} (1 + 0.2 M^2)^{-3} \left(\frac{6M^2}{M^2+5} \right)^{-7/2} \left(\frac{6}{7M^2-1} \right)^{-5/2}$$

and $\mu_u(T_t)$ is given by Sutherland's viscosity law.

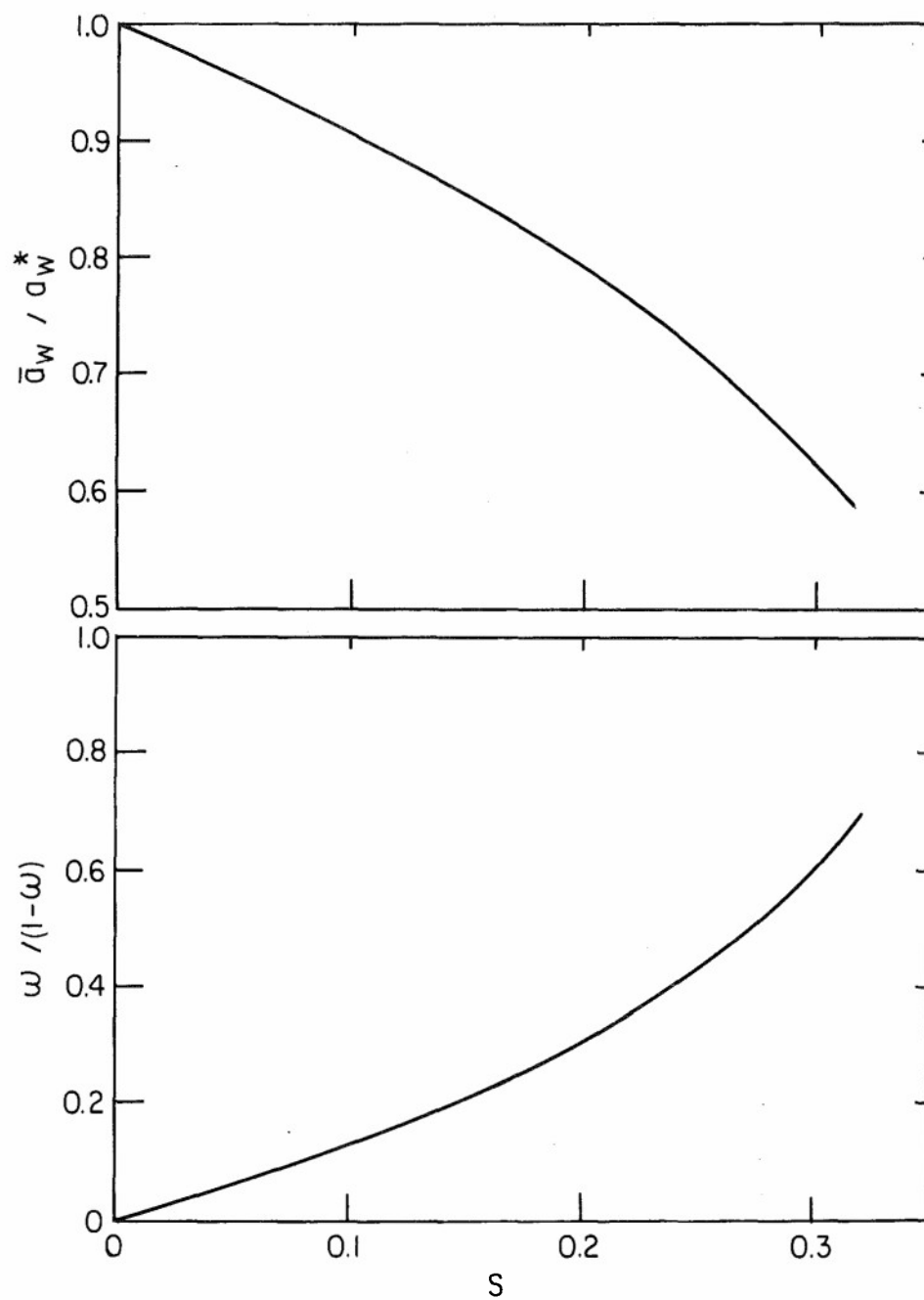


FIG. A-1 END LOSS CORRECTION FACTORS